

Laboratory study of the interaction between two internal wave rays

By S. G. TEOH, G. N. IVEY AND J. IMBERGER

Department of Environmental Engineering, Centre for Water Research,
The University of Western Australia, Nedlands, Western Australia 6907

(Received 21 August 1995 and in revised form 4 October 1996)

Laboratory experiments were conducted to study the interaction between two downward propagating internal wave rays with identical properties but opposite horizontal phase velocities. The intersection of the rays produced a velocity field with stagnation points, and these points propagated vertically upwards within the intersection region. Nonlinear non-resonant interactions between the two rays produced evanescent modes, with frequencies greater than the ambient buoyancy frequency, trapped within the intersection region. These evanescent modes provided a mechanism whereby energy could accumulate locally and, even though the vertical wavelength of the primary resultant wave remained the same, the local isopycnal displacements increased in time. Eventually, the isopycnals were forced to overturn in the region just above the stagnation points by the variation with depth in the local horizontal strain rate.

The gravitationally unstable overturning ultimately broke down releasing its available potential energy and generating turbulence within the intersection region. The results showed that the release of available potential energy was disrupted by the wave motions and even the dissipative scales were directly affected by the ambient stratification and the background wave motion. The distribution of the centred displacement scales was highly skewed towards the Kolmogorov scale and the turbulent Reynolds number Re_t was low. Thus, the net buoyancy flux was very small and almost all turbulent kinetic energy was dissipated over the parameter range investigated. The results also showed that for such dissipative events the square of the strain Froude number ($\epsilon/\nu N_0^2$) and the turbulent Reynolds number Re_t can be less than one.

1. Introduction

In a stratified lake or ocean, basin scale motions can produce smaller scale internal waves (e.g. Thorpe 1975; Imberger 1994) which distribute momentum and energy throughout the water body (e.g. Müller & Henderson 1991). This wave field, in turn, is an energy source sustaining turbulence and small-scale mixing in the interior of the water body (e.g. Gregg 1987; Ivey & Imberger 1991, hereinafter referred to as II). In this way, internal waves link the energy-containing scales to the dissipative scales (e.g. Munk 1981; Müller, D'Asaro & Holloway 1991; Imberger 1994) and quantifying the internal wave dynamics is thus of great importance in the fields of physical limnology and oceanography.

The properties of internal waves have been well documented (e.g. Phillips 1977) and their propagation in a linearly stratified water has been clearly visualized in schlieren pictures by Mowbray & Rarity (1967). As the waves propagate in a stratified fluid, they

can be trapped either between two turning points within a thermocline (e.g. LeBlond & Mysak 1978; Garrett & Munk 1979; Javam, Imberger & Armfield 1997*a*) or by a spatially periodic current (Phillips 1968). Alternatively, they can be absorbed at a critical level (e.g. Thorpe 1981; Winters & Riley 1992; Lin *et al.* 1993*a*; Javam *et al.* 1997*a*). Further, they can break on a sloping bottom, generating either localized unstable density structures near the slope (Thorpe 1987*a*), turbulence in the vicinity of the bottom (Ivey, DeSilva & Imberger 1995), or drive boundary mixing (e.g. Ivey & Nokes 1989, hereinafter referred to as IN; Taylor 1993). Besides these effects, at the depth where two downward propagating internal wave rays intersect, nonlinear non-resonant interactions between the two rays can generate instability and ‘traumata’ (McEwan 1973; Javam *et al.* 1995*b*).

The effect of resonant interactions on internal waves has received some attention in the literature (e.g. Thorpe 1966, 1987*a*; Martin, Simmons & Wunsch 1969, 1972; Phillips 1977; Lin *et al.* 1996) as nonlinear resonant interactions provide a mechanism to transfer wave energy across the frequency (and wavenumber) spectrum. Resonant interactions may also cause the amplitude of parasitic waves to grow once the amplitude of host waves exceeds a critical value (McEwan 1971). Eventually, an instability occurs and the ambient stratified water is mixed (e.g. McEwan 1971, 1983*a, b*; Taylor 1992). In contrast, nonlinear non-resonant interactions have received relatively little attention (e.g. McEwan 1973; McEwan & Plum 1977; Thorpe 1987*a*), even though they also transfer wave energy across the spectrum and the criterion for their occurrence is less restrictive (Phillips 1977).

Suppose two plane internal waves are interacting nonlinearly, and each of them is governed by the dispersion relation (e.g. Phillips 1977)

$$\left(\frac{f}{N_0}\right)^2 = \left(\frac{k_h}{k}\right)^2 = \cos^2 \theta, \quad (1)$$

where f is the wave frequency, k is the wavenumber, and θ is the angle between the wavenumber vector $\mathbf{k} = (k_h, k_v)$ and its horizontal component $(k_h, 0)$;

$$N_0^2 = -(g/\rho_0) d\bar{\rho}/dz$$

is the square of the ambient buoyancy frequency where $\rho(x, z, t) = \rho_0 + \bar{\rho}(z) + \tilde{\rho}(x, z, t)$ is the instantaneous density structure, ρ_0 is the constant reference density (the average density of the water column), $(\rho_0 + \bar{\rho}(z))$ is the quiescent ambient density, and $\tilde{\rho}(x, z, t)$ is the wave density fluctuations about the ambient density.

Further, assume that nonlinear interaction produces a third wave. If the frequencies and wavenumbers for the three waves are related by

$$f_3 = f_1 \pm f_2, \quad \mathbf{k}_3 = \mathbf{k}_1 \pm \mathbf{k}_2, \quad (2a, b)$$

and the third wave is also governed by the dispersion relation (1), then a triad resonant interaction is formed (e.g. Thorpe 1966; McComas & Bretherton 1977; Phillips 1977; Lin *et al.* 1993) and wave energy is transferred towards frequencies lower than the forcing frequency (e.g. Martin *et al.* 1969, 1972; McEwan 1971; McEwan & Robinson 1975). Any resonant triad consisting of a finite-amplitude wave and two infinitesimal components is unstable for the sum interaction and neutrally stable for the difference interaction (Hasselmann 1967; McEwan 1971). Note that each of the three waves participating in a resonant triad is an exact solution of the equation of motion (with the inviscid and Boussinesq assumptions).

On the other hand, if the third wave fails to satisfy the resonant conditions (equations (1) and (2)), it becomes a forced oscillation sustained by the nonlinear terms in the equation of motion. In this case, nonlinear non-resonant interactions are

responsible for transferring energy to the third wave if the two original waves have some finite amplitude (e.g. McEwan 1973). Since each of the two original waves is an exact solution of the equation of motion, their amplitudes are theoretically unconstrained (neglecting the possibility of hydrodynamic instability). Therefore, this finite-amplitude criterion is, in general, less stringent than the resonant conditions (Phillips 1977).

For the case of two internal waves having the same frequency passing through each other in a linearly stratified fluid, Phillips (1968) has concluded from a theoretical study that the waves do not interact. The experiments described below show, however, they can in fact interact, leading to the production of modes which have frequencies greater than the ambient buoyancy frequency and ultimately the generation of gravitationally unstable overturning.

While nonlinear interactions distribute wave energy across the frequency (and wavenumber) spectrum, instabilities initiate the transition to turbulence, leading to an energy cascade to even smaller scales. Recent work (Taylor 1992; Winters & Riley 1992; Lombard & Riley 1996) has shown that a rich variety of instabilities can simultaneously occur in an internal wave field preceding the occurrence of turbulence. These instabilities can include both shear instability (e.g. Turner 1973; Thorpe 1987*b*; Lawrence, Browand & Redekopp 1991) and gravitational instability (e.g. Orlanski & Bryan 1969; Delisi & Orlanski 1975; McEwan 1983*a*; Thorpe 1994*a, b*). For the case of gravitational instability, the mechanism leading to the transition from the wave motion to localized unstable density structure, followed by turbulence, is often ambiguous (Thorpe 1994*b*).

The instantaneous turbulent kinetic energy (TKE) dissipation rate ϵ can be normalized by viscosity ν and N_0^2 . Recently, $\epsilon/\nu N_0^2$ has been discussed widely in the literature (e.g. Stillinger, Helland & Van Atta 1983; Gargett 1988; Yamazaki 1990; Phillips 1991; Imberger 1994). In stratified turbulence, the scales at which energy is fed into turbulence are often assumed to be of the order of either the Ozmidov scale $L_0 = (\epsilon/N_0^3)^{1/2}$ or the overturning scale derived from density measurements (e.g. Thorpe 1977; Gargett, Osborn & Nasmyth 1984; Hopfinger 1987; Luketina & Imberger 1989; Gibson 1991; Taylor 1992). With the former assumption, $\epsilon/\nu N_0^2$ indicates the separation between the energy-containing scales and the Kolmogorov scale $L_k = (\nu^3/\epsilon)^{1/4}$ (Gargett *et al.* 1984; Phillips 1991). Thus, does $(\epsilon/\nu N_0^2) = (L_0/L_k)^{4/3}$ have a lower limit of $O(1)$ because L_k is the smallest lengthscale for turbulent velocity fluctuations? With the latter assumption, II defined the turbulent Reynolds number $Re_t = (\hat{L}_c/L_k)^{4/3}$ where \hat{L}_c is the root mean square centred displacement scale. Again, Re_t is a measure of the separation in scales. Hence, does Re_t have the same lower limit? The present laboratory experiments have attempted to address some of the questions raised above by investigating the consequences of nonlinear non-resonant interactions between two downward propagating internal wave rays having identical properties but opposite horizontal phase velocities.

2. Laboratory experiments

The experiments were performed in a glass tank 5900 mm long, 535 mm wide and 540 mm deep (figure 1). At each end of the tank, sloping bottoms at an angle of 20° to the horizontal floor were installed as wave absorbers. Internal waves with frequencies exceeding the critical frequency of $0.34 N_0$ would thus forward reflect off the slopes towards the apexes where they were dissipated (e.g. Turner 1973; Cacchione & Wunsch 1974), leaving the working section free from end-wall reflections. The tank

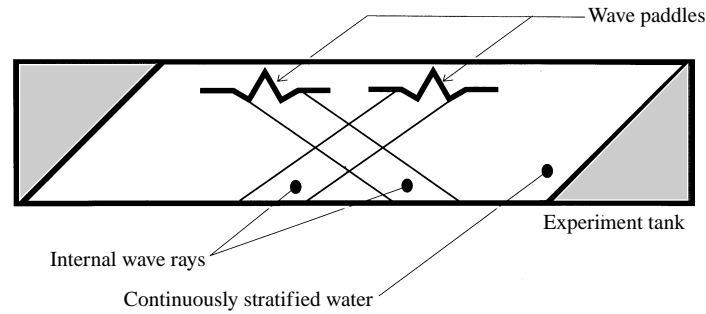


FIGURE 1. Schematic of the experiment tank (elevation view). Support and eccentric crank-driving arm mechanisms for wave paddles are not shown.

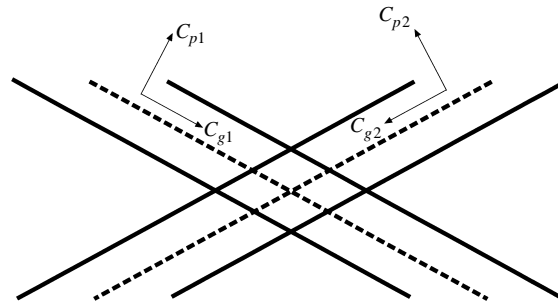


FIGURE 2. Schematic of the two rays generated by the two paddles. Solid lines are the maxima wave-induced density fluctuations (wave crests); dashed lines are the minima wave induced density fluctuations. C_{p1} and C_{p2} are phase velocities, and C_{g1} and C_{g2} are the group velocities.

was filled with a linearly stratified salt water by using the two-tank technique (Fortuin 1960).

Two identical wave-paddles, driven by a d.c.-motor, were located horizontally near the centre of the tank at 40 mm below the free surface to generate two internal wave rays (McEwan 1973; Teoh 1995). These paddles were separated, centre to centre, by 615 mm and each consisted of eight blades which could pivot independently about their long central axes (figure 1). During the experiments, only the central six blades were oscillated, thus forming either an M or W shape with a total width of 286 mm, and the two emitted waves had a width of 1.5 times the wavelength. The central amplitude of each paddle was 20 mm, while the amplitudes at both sides of the paddles were set at half the central amplitude in order to minimize the net volume flux induced by blade displacements.

The intersection between the two rays was visualized by bull eye's rainbow schlieren and shadowgraph techniques (Merzkirch 1974), in conjunction with velocity measurements made by particle image velocimetry. A 23 mm diameter bull's eye rainbow filter consisting of concentric annuli of rainbow colours, with the colour blue at the core, was used in the set up for the rainbow schlieren technique (Howes 1984; IN). Particle image velocimetry was carried out by injecting Pliolite particles of less than 75 μm into the flow field. These suspended particles were illuminated with a 5 mm thick vertical light sheet, created from a 1000 W white theatre lamp. Particle images were recorded at 25 frames per s with a black and white CCD camera and a Super-VHS video recorder. Pairs of particle images, each integrated over two consecutive frames, were digitized at 5 frame intervals apart using an image acquisition system. To derive two-dimensional velocity fields, each pair of images was analysed by the maximized

cross-correlation (MCC) technique described by Stevens & Coates (1994), employing a window of 45×45 pixels (8.8 mm horizontally \times 8.6 mm vertically). The vertical shear was then computed from the velocity fields by using a three-point centre differencing scheme, and a Butterworth filter was used to eliminate fluctuations with wavelength smaller than 8.6 mm.

Vertical density profiles and time series measurements were obtained with a combination of a Precision Measurement Engineering (PME) siphoning conductivity probe (SCP), a four-electrode fast response micro-conductivity probe (FRC) (Head 1983) and a fast response thermistor of nominal resistance 100 k Ω (FP07). Since the SCP drifted less than 0.2% over 10 h, the FRC conductivity was calibrated *in situ* against the SCP conductivity thereby compensating for any drift in the FRC. The response time for the FRC and FP07 were, respectively, 4 ms and 12 ms. The roll-off for the FP07 was digitally corrected to 4 ms using the methods described in detail by Fozdar, Parker & Imberger (1985). Profiling was done at a vertical traverse speed of 100 mm s⁻¹ and the direct and differentiated output from each sensor was collected at 100 Hz through a 16-bit analog-digital converter.

3. Flow visualization

3.1. Rainbow colour schlieren pictures

A schematic of the two rays generated by the paddles is shown in figure 2. Within the rays, the wave crests (defined as the maximum $\tilde{\rho}$) propagate obliquely upwards at the phase velocity; on the other hand, the energy propagates obliquely downwards at the group velocity (e.g. Phillips 1977). Note that the two rays have identical horizontal and vertical wavelengths.

Figure 3 shows a sequence of schlieren images in the region of intersection of the two rays. The quiescent ambient fluid was linearly stratified and the field of view initially blue in colour (from the video images). When the paddle started moving, the energy of the two rays propagated downward and intersected for the first time at $1.3T$, where T was the wave period. Within the intersection, the wave-induced density gradient fluctuations revealed by the schlieren colour scheme grew and eventually developed a regular pattern propagating vertically upwards (e.g. figure 3(a) taken at $4.4T$). The density gradient fluctuations in figure 4(a) are symmetric about the horizontal and the vertical axes. As the rays continued to interact, symmetrical forcing about the vertical axis maintained the symmetry about the vertical axis (e.g. figure 3(b) taken at $11.3T$); however, the local production of smaller-scale flow features created asymmetry about the horizontal axis. The smaller-scale flow features were only observed in the upper half of figure 3(b), suggesting a fraction of the wave energy must have been trapped in this region.

Figure 3(c) (taken at $14.9T$) shows the appearance of a turbulent patch consisting of small-scale filaments along the horizontal axis near the centre of the image. A black coloured region was observed to surround this patch, indicating a strong density gradient boundary. Note that the portion of the flow field which is black occupied a larger area in the upper half of the figure as compared to the lower half of the figure. This indicates that the wave-induced density gradient fluctuations were, on average, larger in magnitude in the upper half of the figure and again suggesting that wave energy had somehow been trapped in the upper half of the image. Later at $15.4T$ (figure 3d), the density field retained its symmetry about the vertical axis and the wave crests continued to propagate vertically upwards. The turbulent patch at the centre of image was strained by the wave motions, going through a cycle of horizontal compression

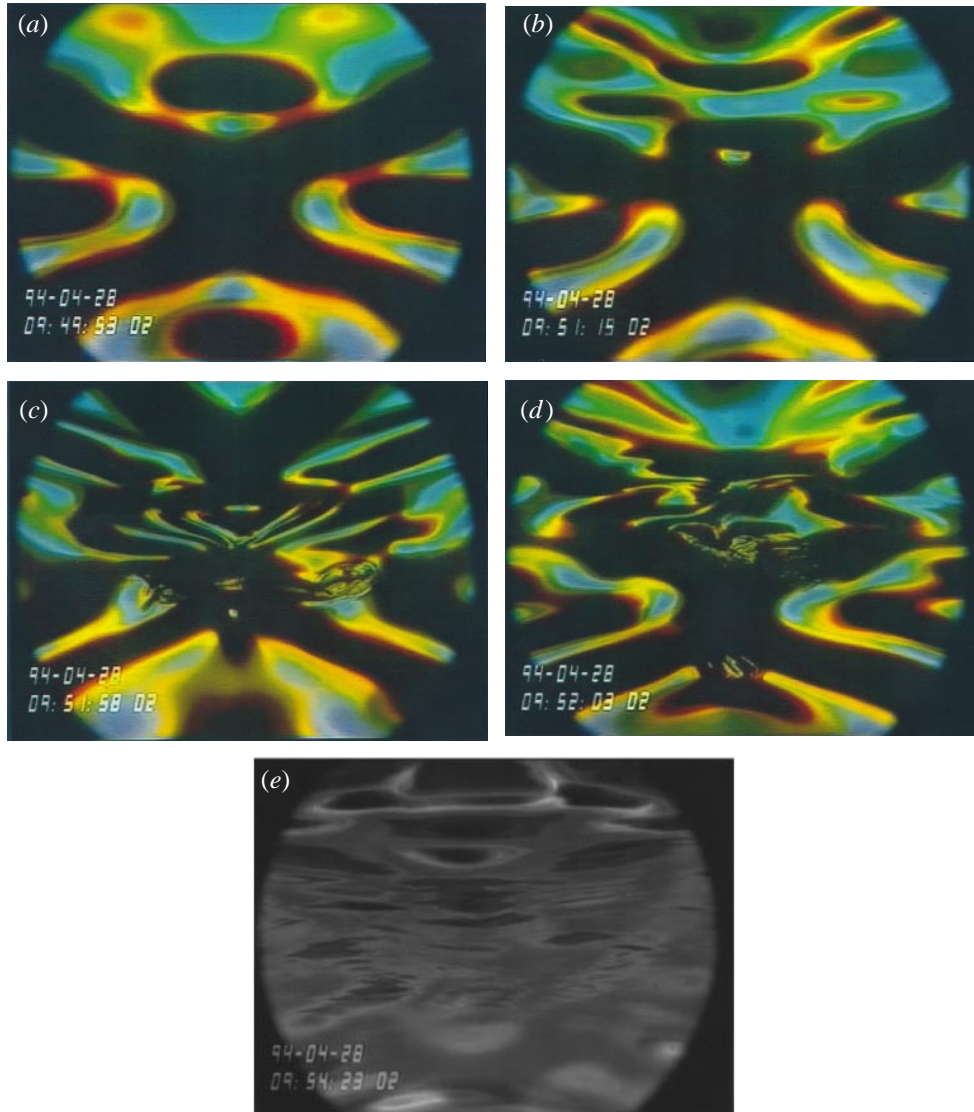


FIGURE 3. Time sequence of rainbow colour schlieren pictures from the experiment with the ambient buoyancy frequency $N_0 = 1.04 \text{ rad s}^{-1}$ and the wave frequency $f = 0.53 \text{ rad s}^{-1}$, making $f/N_0 = 0.49$. Based on these parameters and the horizontal width of the paddles in motion, the height of intersection was 161 mm, and the width was 286 mm. The field of view had a vertical dimension of 154 mm and diameter 300 mm. The two paddles were above the photographs. The photos were taken from the video images at (a) $4.4T$, (b) $11.3T$, (c) $14.9T$, and (d) $15.4T$; (e) was taken at $4T$ after the paddles stopped.

with vertical extension and then vice versa, although the centroid of the patch remained fixed in space. Once the forcing stopped, the turbulent patch collapsed, intruding horizontally into the surrounding fluid and eventually relaminarized (figure 3e).

3.2. Shadowgraph pictures

While the shadowgraph method has a reduced sensitivity compared to the schlieren method, the considerably larger field of view assisted in the interpretation of the wave interactions. Figure 4(a) shows a shadowgraph picture taken from the video

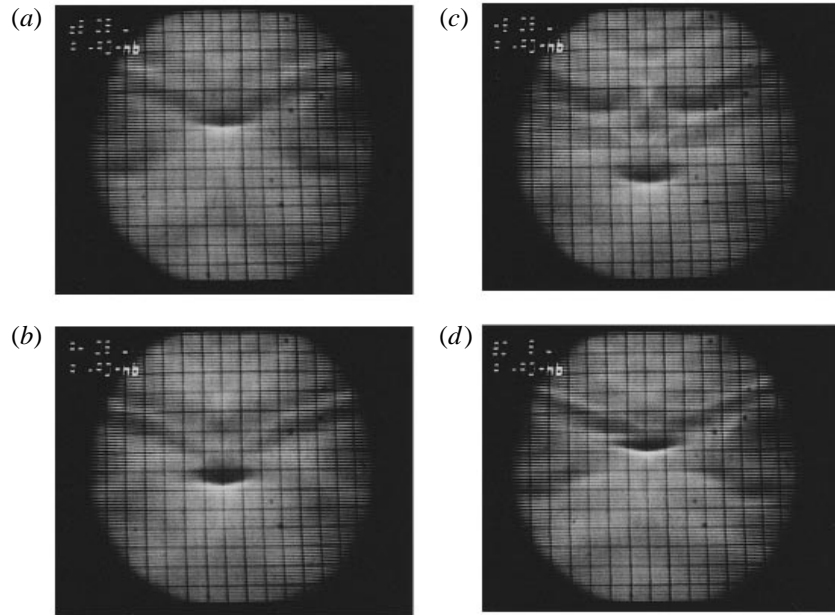


FIGURE 4. Time sequence of shadowgraph pictures from the experiment with the ambient buoyancy frequency $N = 1.27 \text{ rad s}^{-1}$ and the wave frequency $f = 0.65 \text{ rad s}^{-1}$, making $f/N_0 = 0.51$. Based on these parameters and the horizontal width of the paddles in motions, the height of the intersection was 170 mm, and the width was 286 mm. The field of view was 300 mm in diameter. The grid lines were 20 mm apart. The top grid lines on the photos were 60 mm below the two paddles. The edge of the left-hand paddle was 20 mm from the left-hand edge of the circular view, and the edge of the right-hand paddle was 40 mm from the right-hand edge. The centreline between the two paddles was 140 mm from the left-hand edge of the circular view. The photos were taken from the video images at (a) $10.2T$, (b) $11.0T$, (c) $11.8T$, and (d) $13.2T$.

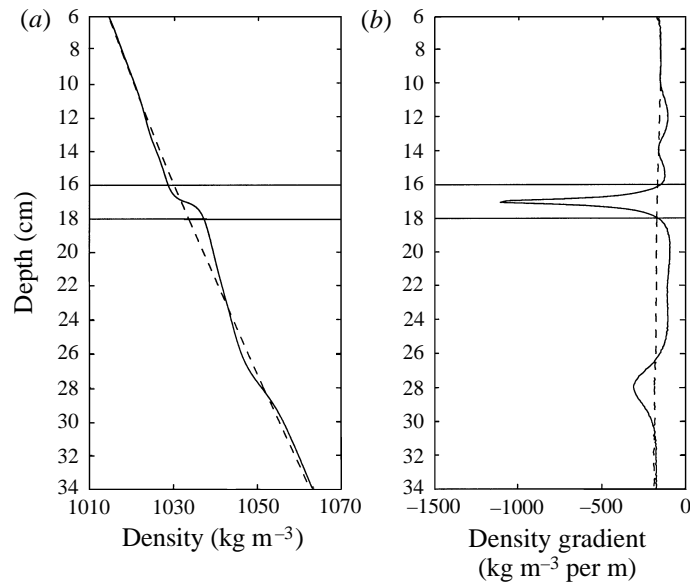


FIGURE 5. Vertical profiles of (a) density and (b) density gradient taken along the centreline between the two paddles at $10.2T$. The dashed line in (a) is the ambient density and the dash line in (b) is the ambient density gradient. Negative density gradient is stable.

images at $10.2T$. Within the intersection region between the two rays and near the centre of the image there was a horizontally elongated area of sharp transition from black to white. Vertical profiles of density and density gradient (§4) taken along the centreline of the intersection region are plotted in figure 5 and the sharp transition area in figure 4(a) was enclosed between the two horizontal lines in figure 4. These two figures demonstrate that the black area in figure 4(a) corresponded to a region where the density gradient had been increased by wave straining. Light that had originally fallen onto this area in a quiescent fluid was deflected downwards and concentrated onto the horizontal white line below the black area, forming the sharp transition from black to white and the wave crest was inside the black area.

Two rays (indicated by grey colour stripes) coming into the intersection region are seen on the upper half of figure 4(b) (taken at $11.0T$). Although the same stripes were also anticipated for the outgoing rays, $\nabla^2\rho$ fluctuations in the rays were weak, causing ambiguity in the image. The weaker $\nabla^2\rho$ fluctuations (to which the shadowgraph is sensitive) in the outgoing rays were the result of some wave energy being trapped inside the intersection region.

Later at $11.8T$ (figure 4c), a new mode (indicated by the diamond-shaped grey region) appeared near the centre of the image at a depth of 180 mm. From the video images, this mode was produced locally and was stationary and below the new mode there was a wave crest that was propagating upwards. This propagating wave and the new stationary mode eventually met and interacted to induce higher $\nabla^2\rho$ fluctuations, indicated by the area of sharp transition from black to white with sharper contrast, in figure 4(d).

The sequence continues in figure 6 where at $13.4T$ a Y-shaped white patch had formed (e.g. figures 6(a) and 6(b) taken at $13.5T$ and $13.7T$, respectively). At the top of the Y-shaped patch, the density field had overturned (§4); as a result, $\nabla^2\rho$ fluctuations were large in magnitude and varied widely, leading to the downwards deflection of the incident light beam and the formation of the vertical white line of the Y-shape. Before the disappearance of this patch, the next wave crest with large $\nabla^2\rho$ fluctuations appeared below the patch (figure 6(c) taken at $13.9T$). Once the first Y-shaped patch disappeared, the second was generated (e.g. figure 6(d) taken at $14.3T$). A similar cycle repeated, but the local $\nabla^2\rho$ fluctuations were even larger (indicated by sharper contrast) (e.g. figure 6d-f). Figure 6(g-i) illustrates the evolution of the third Y-shaped patch which eventually degenerated into a more complex structure than on the previous cycle. Localized thin elongated filaments were formed, resembling fine structure within the ‘hard-line traumata’ described by McEwan (1973).

The turbulent fluctuations after overturning are not obvious in figure 6. This was partly due to the finite dimension of the light source used in the set-up for the shadowgraph method (Merzkirch 1974). Moreover, the presence of intense white light within the Y-shaped patch, the lack of image sharpness and contrast, together with the integral effects of the shadowgraph all contributed to the reduction in the sensitivity of the shadowgraph pictures compared to the schlieren images in figure 4.

Results from figures 3, 4 and 6 appear to contradict the theoretical prediction of Phillips (1968) that two internal waves of the same frequency pass through each other unaffected. Phillips’ (1968) findings, however, were based on a two-scale perturbation analysis and are only valid for weakly nonlinear interactions. In contrast, the results shown in figures 3, 4 and 6 involved strong nonlinear non-resonant interactions (§4 and see also Javam *et al.* 1997a, b). This was demonstrated in preliminary experiments using two wave-paddles similar to those discussed in §2, but with the central amplitudes of only 10 mm and a wavelength of 88 mm. These experiments showed only

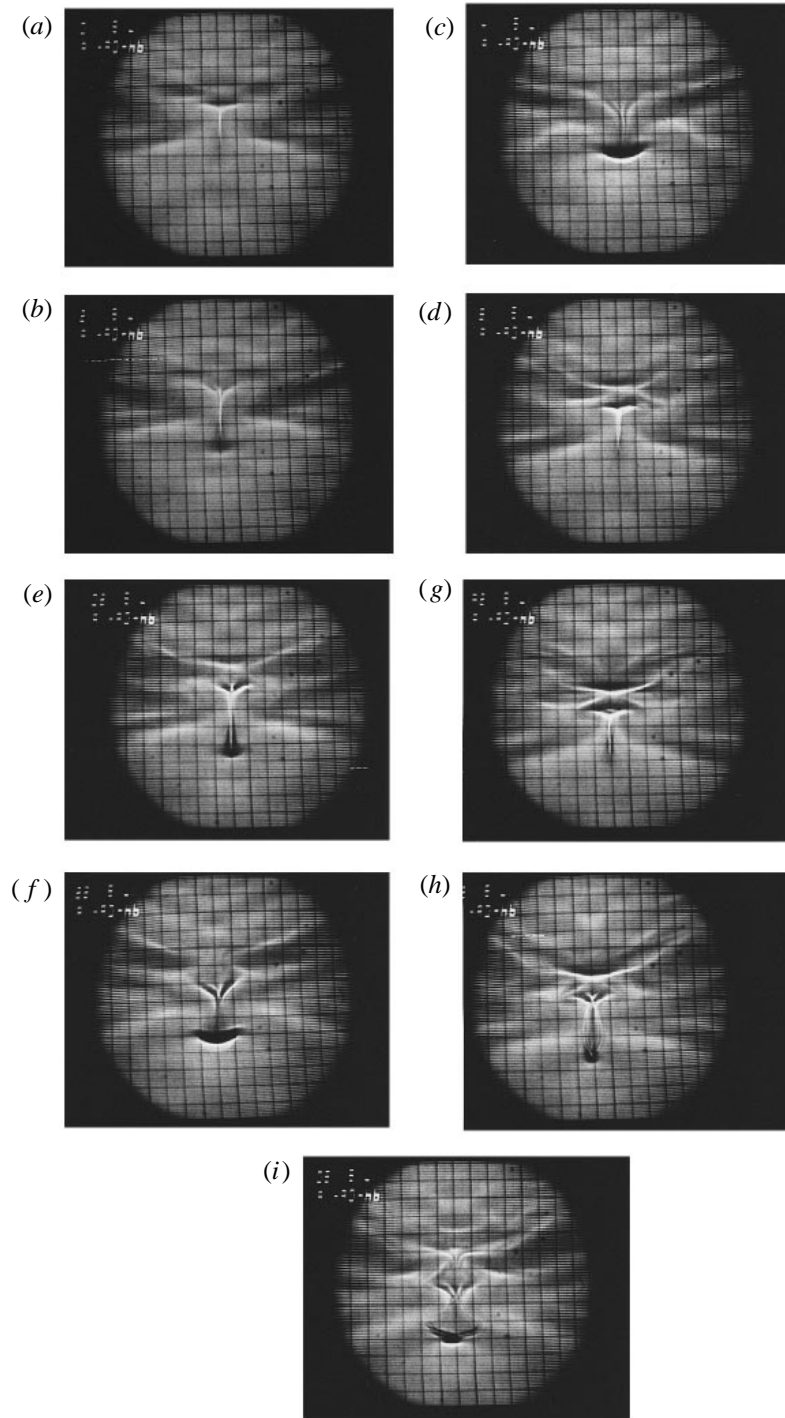


FIGURE 6. Same as figure 4, but the photos were taken from the video images at (a) $13.5T$, (b) $13.7T$, (c) $13.9T$, (d) $14.3T$, (e) $14.5T$, (f) $14.7T$, (g) $15.1T$, (h) $15.3T$, and (i) $15.5T$.

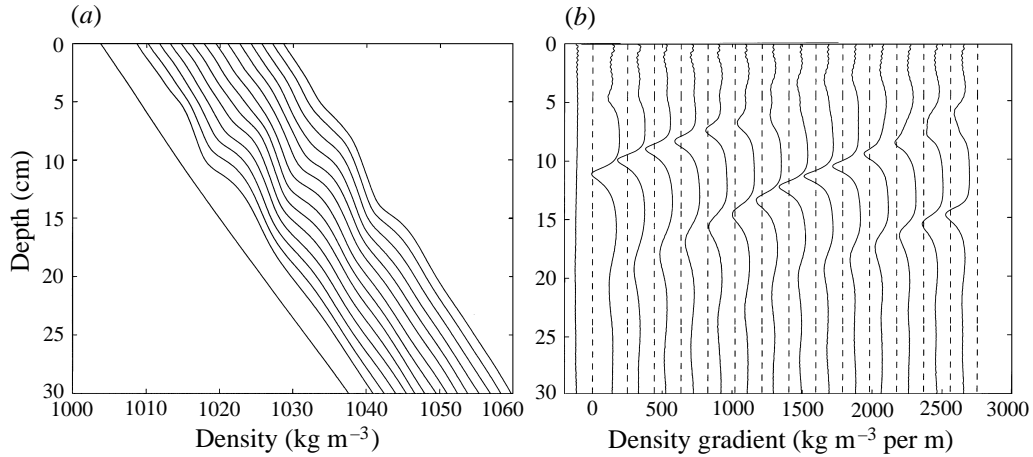


FIGURE 7. Vertical profiles of (a) density and (b) density gradient taken between $3T$ and $4.6T$ at $(0.12 \pm 0.03)T$ apart from the series of repeated experiments with the ambient buoyancy frequency $N_0 = 1.05 \text{ rad s}^{-1}$, the wave frequency $f = 0.385 \text{ rad s}^{-1}$, making $f/N_0 = 0.37$. The leftmost profile was taken through a quiescent ambient water. The scales on the horizontal axis were correct for the leftmost profile; subsequently, profiles were offset by constants proportional to the time interval apart, respectively (except the first offset). Zero depth referred to the first sample. In (b), dashed lines correspond to the zero gradient. The high-wavenumber fluctuations at the top of the gradient profiles were induced by mechanical vibrations during the start-up of traverse motions. These vibrations decayed before the sensors entering the intersection region as observed on the first profile. Estimating from the profiles, the vertical wavelength was 73 mm , and the upwards vertical phase velocity was 5.5 mm s^{-1} .

regular patterns similar to figure 3(a) within the intersection but the pattern remained unchanged with time. The video images of these runs indicated no sign of local production of smaller-scale flow features, in agreement with the theory of Phillips (1968). As figures 3–6 clearly show, there exists a threshold amplitude beyond which strong nonlinear non-resonant interactions can occur.

4. Evolution of the density field

4.1. Vertical profiles

To complement the results of flow visualizations, density and density gradient profiles were taken to examine the evolution of the density profiles towards gravitationally unstable density structures. By repeating experiments with the same parameters but profiling at different times, a series of vertical profiles was obtained along the centreline of the intersection. Figure 7 shows the vertical profiles in the time interval from $3T$ to $4.6T$. The resultant wave, isolated within the intersection region, was propagating vertically upwards. Although the upper portion of the density gradient profiles after $4.4T$ was distorted, the density fluctuations were clearly dominated by a single mode wave, as anticipated from visualization.

Figure 8 shows density profiles in the progression towards gravitationally unstable overturning from $4.2T$ to $15.2T$. These profiles were taken at approximately the same phase (i.e. one wave period apart) from experiments with a higher wave frequency and ambient buoyancy frequency than those in figure 7. The density profile taken at $8.3T$ (the sixth profile) shows the presence of the primary resultant wave and the locally produced new modes (see §4.2 below) which had shorter vertical wavelengths. As a result, a double peak was formed in the density gradient profile at depth of 170 mm .

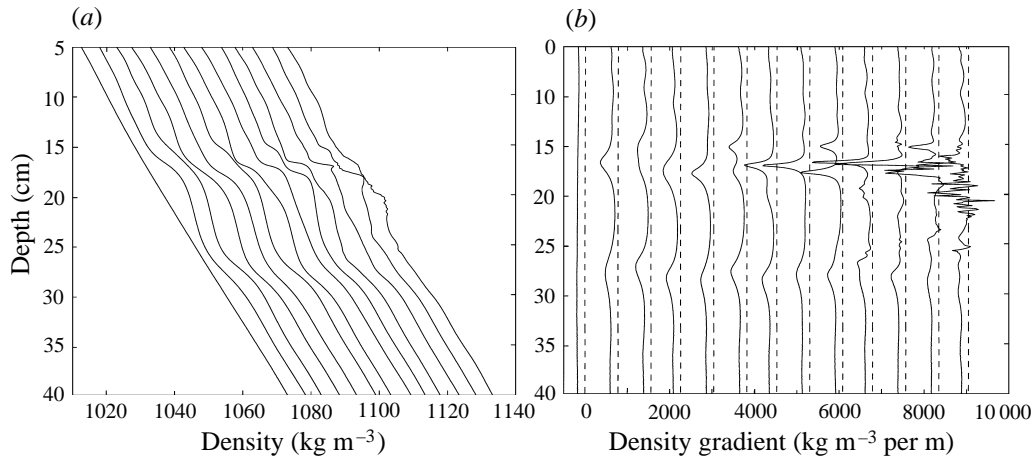


FIGURE 8. Vertical profiles of (a) density and (b) density gradient taken between $4.2T$ and $15.2T$ at $(1.00 \pm 0.07)T$ apart from the series of repeated experiments with the ambient buoyancy frequency $N_0 = 1.26 \text{ rad s}^{-1}$, the wave frequency $f = 0.65 \text{ rad s}^{-1}$, making $f/N_0 = 0.51$. The first profile was taken through a quiescent ambient water. The scales on the horizontal axis were correct for the leftmost profile; subsequently, profiles were offset by constants proportional to the time interval apart, respectively (except the first offset). Zero depth referred to the paddles' level. In (b), dashed lines correspond to the zero gradient.

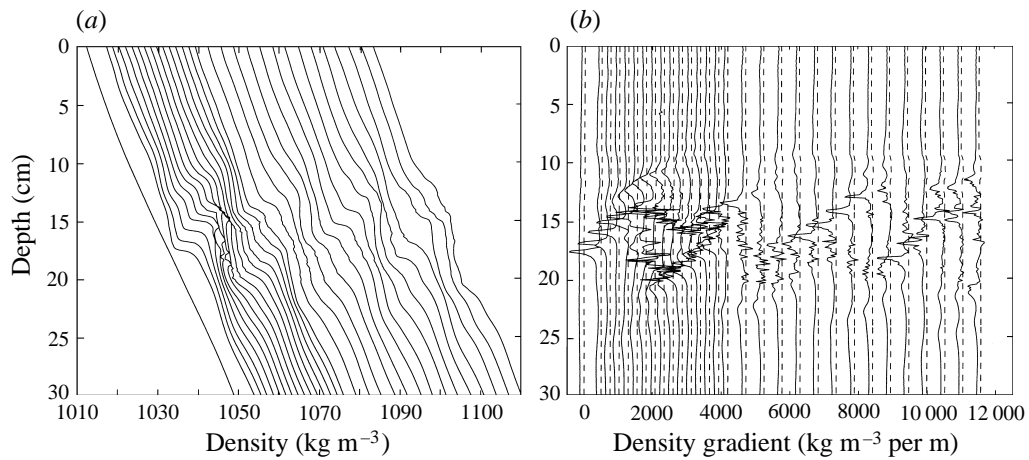


FIGURE 9. Vertical profiles of (a) density and (b) density gradient taken between $13.92T$ and $15.10T$ at $(0.08 \pm 0.01)T$ apart and between $15.10T$ and $17.45T$ at $(0.17 \pm 0.01)T$ apart from the series of repeated experiments with the ambient buoyancy frequency $N_0 = 1.1 \text{ rad s}^{-1}$, the wave frequency $f = 0.53 \text{ rad s}^{-1}$, making $f/N_0 = 0.48$. The first profile was taken through a quiescent ambient water. The scales on the horizontal axis were correct for the leftmost profile; subsequently, profiles were offset by constants proportional to the time interval apart, respectively (except the first offset). Zero depth referred to the paddles' level. In (b), dashed lines correspond to the zero gradient.

On the two succeeding profiles (taken at $9.2T$ and $10.2T$), the peak at a depth of 170 mm abruptly increased in magnitude as the primary resultant wave propagated past the new mode.

A double peak in the gradient profile reappeared at $11.3T$, but this time with larger values than those observed earlier. At $12.2T$, fluctuations with distinctly smaller wavelengths appeared for the first time in two isolated regions in the neighbourhood

of the peak density gradients. By this time, the peak density gradient at depth 170 mm had intensified to 2.8 times the value at five wave periods earlier. A period later (at $13.2T$), the density field overturned at a depth immediately below the peak density gradient. This peak density gradient was within the region of sharp transition from black to white on figure 4(d) (see also figure 6). The last profile taken at $15.2T$ demonstrates that gravitationally unstable overturning eventually broke down to produce small-scale turbulent fluctuations, although note that the density gradient profile shows only a few zero-crossings.

These small-scale turbulent fluctuations after overturning were examined in more detail by taking vertical density and density gradient profiles during $13.92T$ and $17.45T$ at a shorter interval between profiles than used in figure 8. Figure 9(a) shows an overturning at $14.17T$ (the fourth profile). It evolved into a large overturning by the next profile taken at $14.26T$. Small-scale turbulent fluctuations formed and persisted thereafter as shown by the density gradient profiles in figure 9(b). From $14.34T$ to $14.85T$, two regions of turbulent density gradient fluctuations were separated by a segment of distinctly smooth density gradient. Initially, the positive rate of change of vertical velocity with height, i.e. $\partial w/\partial z > 0$ (the vertical dilation strain rate), induced by the background internal wave (§5) expanded this separation. As the wave continued to propagate through the small-scale fluctuations, the two regions of turbulent density gradient fluctuations were, in turn, forced together by the negative $\partial w/\partial z$ (i.e. the vertical compressive strain rate). A similar structure was also observed on the next cycle between $16.27T$ and $16.61T$. Turbulent density gradient fluctuations before $15.10T$ were visually more intense than those after this time. Throughout this sequence of profiles, zero-crossings and unstable density gradients were rare.

4.2. Production of new modes

Time series of density fluctuations were collected within an incoming ray, an outgoing ray, and within the intersection region to investigate the production of new modes by nonlinear non-resonant interactions between the two rays. The evolution of the frequency content for an incoming ray and an outgoing ray are shown separately on figures 10 and 11. Note that as the amplitude of the central wave-blades was twice that of the blades at the sides of the paddle, the wave amplitude varied across the beam. As a consequence, the exact spectral levels are different between the two records shown in figures 10 and 11, reflecting the exact locations of the sensors relative to the local centre of the wave beam. Although small peaks at other frequencies were observed, clearly both these spectra from the incoming and outgoing rays were dominated by energy at the forcing frequency $f = 0.1$ Hz.

On the other hand, when the spectra were computed from the time series obtained within the intersection region they showed substantial peaks at $2f$ (i.e. $1.02 N_0$) and $3f$ (figure 12b–d) (cf. Javam *et al.* 1997a, b). Indeed, figure 12(c) shows that the maximum peak was at $2f$. Since the wave energy inside the incoming rays was at the frequency f , the $2f$ and $3f$ components must have been produced locally by sum interactions. Since the new modes had frequencies greater than the ambient buoyancy frequency N_0 , they were not governed by the dispersion relation (1); hence, the new modes were forced oscillations sustained by the nonlinear terms in the equation of motion and do not satisfy the nonlinear resonant conditions in equations (1) and (2). The implication is that nonlinear non-resonant interactions were responsible for transferring the wave energy from the forcing frequency to the new modes.

Figure 13 illustrates the frequency content for the time series collected at a distance 0.22 times the horizontal wavelength away from the centreline of the intersection and

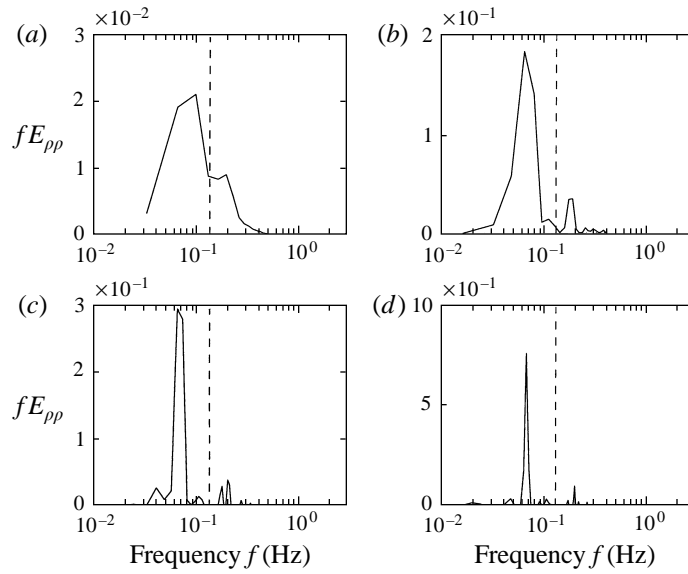


FIGURE 10. Spectra of density fluctuations $E_{\rho\rho}$ ($(\text{kg m}^{-3})^2 \text{Hz}^{-1}$) computed from the time series collected within the incoming ray at, in (x, z) (mm coordinates), $(80, 86)$ with record length of (a) $2.1T$, (b) $4.2T$, (c) $8.5T$ and (d) $17T$. The paddles' level was at depth $z = 0$. The centreline between two paddles was at horizontal distance $x = 0$, increasing positive towards the right paddle. Time series measurements began when the paddle started to oscillate. It was collected at 100 Hz from the experiment with the ambient buoyancy frequency $N_0 = 1.26 \text{ rad s}^{-1}$ and the wave frequency $f = 0.65 \text{ rad s}^{-1}$, making $f/N_0 = 0.51$. The dashed lines on the figure indicate the ambient buoyancy frequency. Spectra were computed from the same time series starting from the first sample, but varying record length, to illustrate the evolution of frequency content. The vertical axis is multiplied by the frequency f . Note the change in the vertical scale.

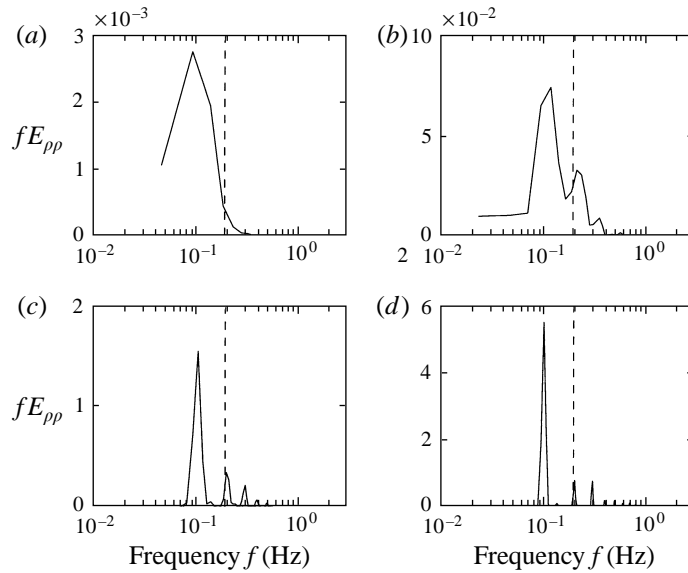


FIGURE 11. Same as figure 10 but from the time series collected within the outgoing ray at $(80, 306)$.

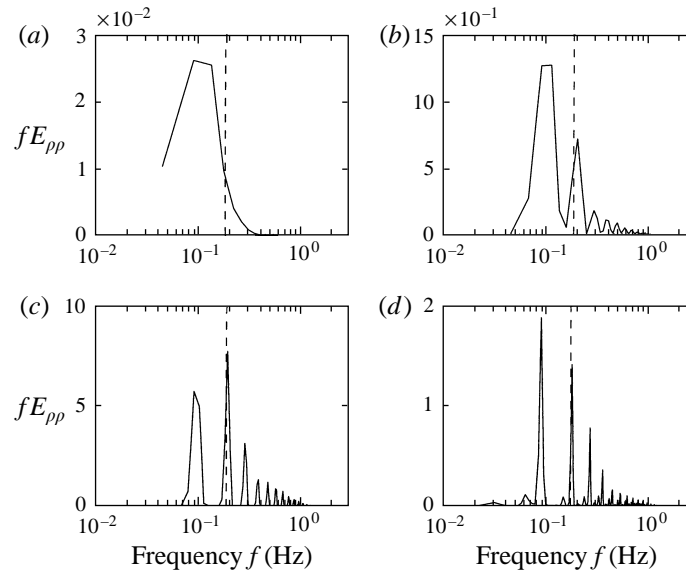


FIGURE 12. Same as figure 10 but from the time series collected at the centreline of the intersection at (0, 196).

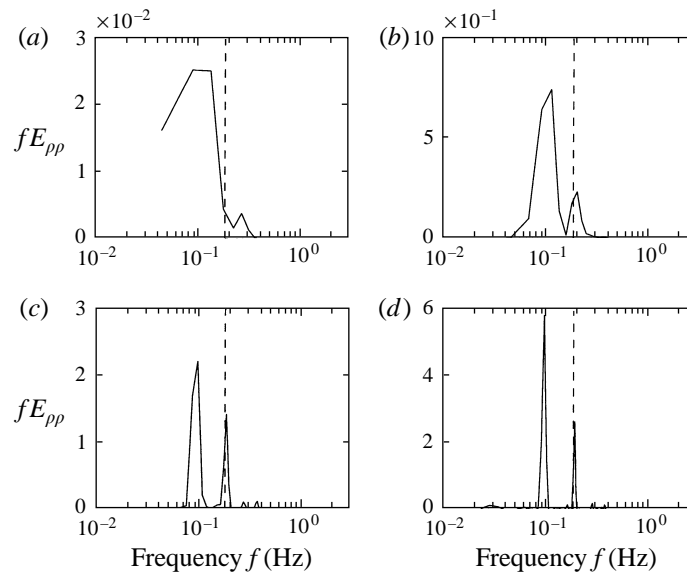


FIGURE 13. Same as figure 10 but from the time series collected away from the centreline of the intersection at (41, 196).

near to the node of isopycnal displacements. Here, the amplitude for the wave induced density fluctuations was smaller than those shown in figure 12. Note also that the spectra show that the wave energy was only transferred to $2f$, suggesting that viscous dissipation had apparently prevented the production of higher-frequency components.

In summary, the new modes with frequencies greater than the ambient buoyancy frequency in figures 12 and 13 are evanescent modes (e.g. LeBlond & Mysak 1978). Not governed by the dispersion relation (1), these modes are forced oscillations which

cannot propagate and therefore the energy transfer from f to the higher-frequency evanescent modes provides a mechanism to accumulate energy locally, leading to larger density fluctuations both above and below the local ambient density. Ultimately, this energy is transferred to small-scale processes (figures 3*c* and 3*d*) by gravitational instability (§6).

5. Evolution of the velocity fields

The velocity fields obtained from the MCC technique between 3.41*T* and 4.45*T* are shown in figure 14. Only the incoming and the outgoing rays to the right of the vertical centreline of the intersection region were measured, although the rays to the left of the centreline would be the mirror image of figure 14. Within the intersection (panel (iii)), velocity fields formed a cellular pattern, exhibiting two distinct stagnation points along the vertical centreline of intersection: one exhibited a horizontal compressive straining (i.e. locally $\partial u/\partial x < 0$), while the second exhibited a horizontal dilation straining (i.e. locally $\partial u/\partial x > 0$). With time, the stagnation points travelled vertically upwards, as seen in the sequence from figures 14(*a*)–14(*d*).

Figure 15 shows the evolution of the velocity fields and Richardson numbers within the intersection between 6.2*T* and 14.3*T*. The velocity fields were measured at about the same phase of the wave cycle. The vertical solid line in the velocity field was the path for the vertical density profiles shown earlier in figure 8. Also shown in panel (i) are the contours for $1/Ri_0$ where $Ri_0 = [N_0/(\partial u/\partial z)]^2$ is the Richardson number based on the ambient stratification; whereas in panel (iii), the Richardson number was defined as $Ri = [N/(\partial u/\partial z)]^2$ where the local $N^2 = -(g/\rho_0)\partial\rho/\partial z$. At those locations where vertical velocities were nearly zero, the wave-induced density fluctuations $\tilde{\rho}(x, z, t) \approx 0$, although the isopycnal displacements were largest near the vertical solid line on panel (i). The ‘true’ instantaneous local Richardson number for the flow field would fall somewhere in between Ri and Ri_0 .

The contour for $1/Ri_0$ in panel (i) in figure 15 suggests that Ri_0 was larger than 0.25 everywhere in the flow before overturning. In addition, vertical profiles for $1/Ri$ were consistently below 4 and became negative when the density field overturned (figure 15*e, f*). Thus, the Richardson number derived from the velocity fields was consistently outside the range between zero and 0.25. Note also that the density overturning was above the stagnation point exhibiting $\partial u/\partial x < 0$ (figure 15*e*) and below the position of maximum velocity and maximum $\tilde{\rho}$. As the vertical shear in the velocity field in the region surrounding the overturning was small before the density was overturned, it is clear that the vertical shear could not have initiated the overturning. Rather, the overturning is best described as a gravitational instability.

The velocity fields shown in figure 15(*b–d*) were clearly distorted by the presence of the evanescent modes, although the pattern of stagnation-point flow remained. The distance between stagnation points was approximately the same, however, and the wavelength of the primary resultant wave remained unchanged. Unlike figure 15(*a*ii), figure 15(*d*ii) shows that the maximum $\tilde{\rho}$ was just below the maximum velocity, suggesting the isopycnal displacements had grown.

As discussed in §4.2, a fraction of the wave energy was trapped within the intersection when it was transferred to the evanescent modes by nonlinear non-resonant interactions. The vertical wavelength of the primary resultant wave remained unchanged and the local isopycnal displacements grew (cf. Javam *et al.* 1997*a, b*). Thus, at some point in time, the variations with depth in $\partial u/\partial x$ would force the isopycnals to overturn above the stagnation point to accommodate their large

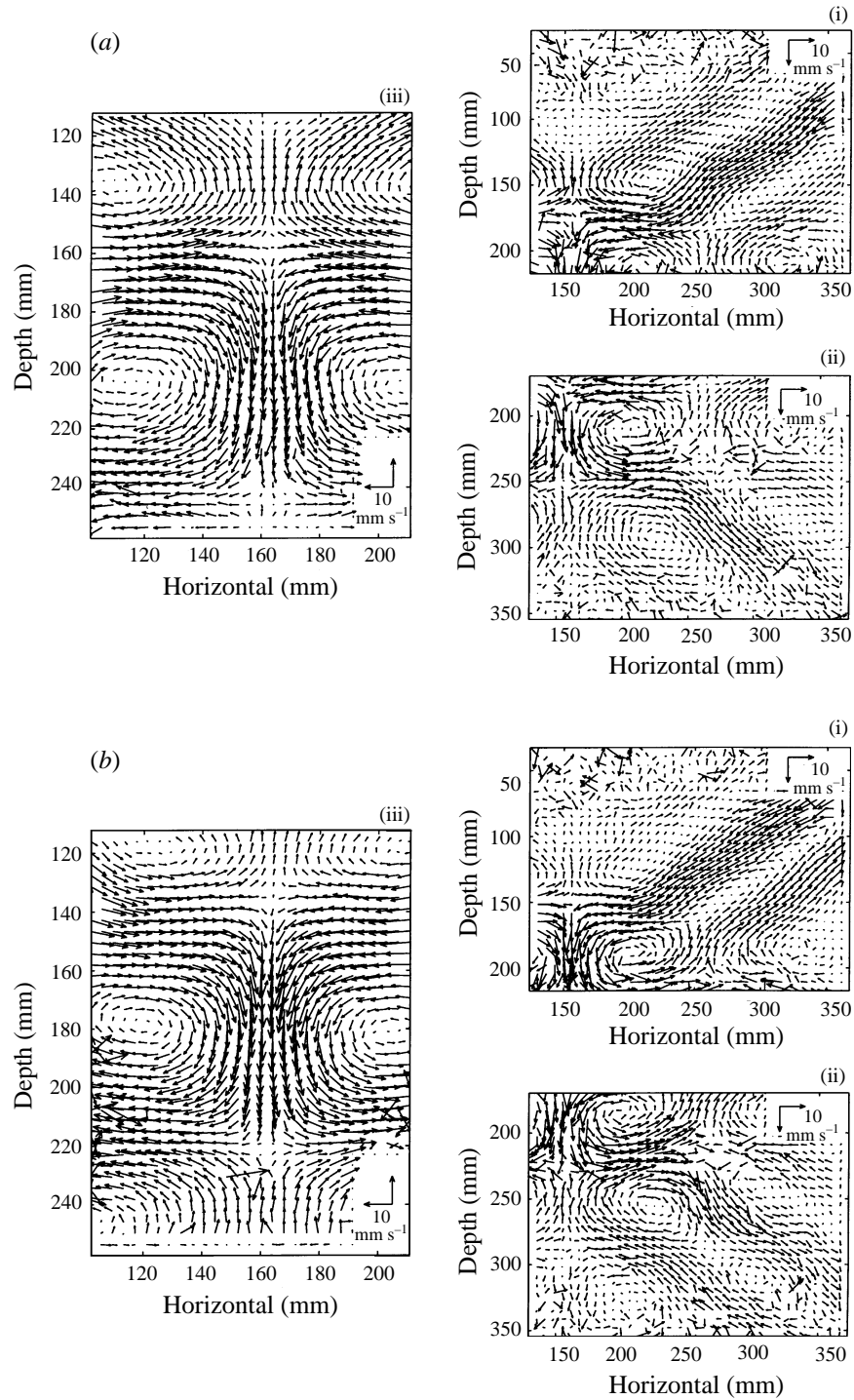
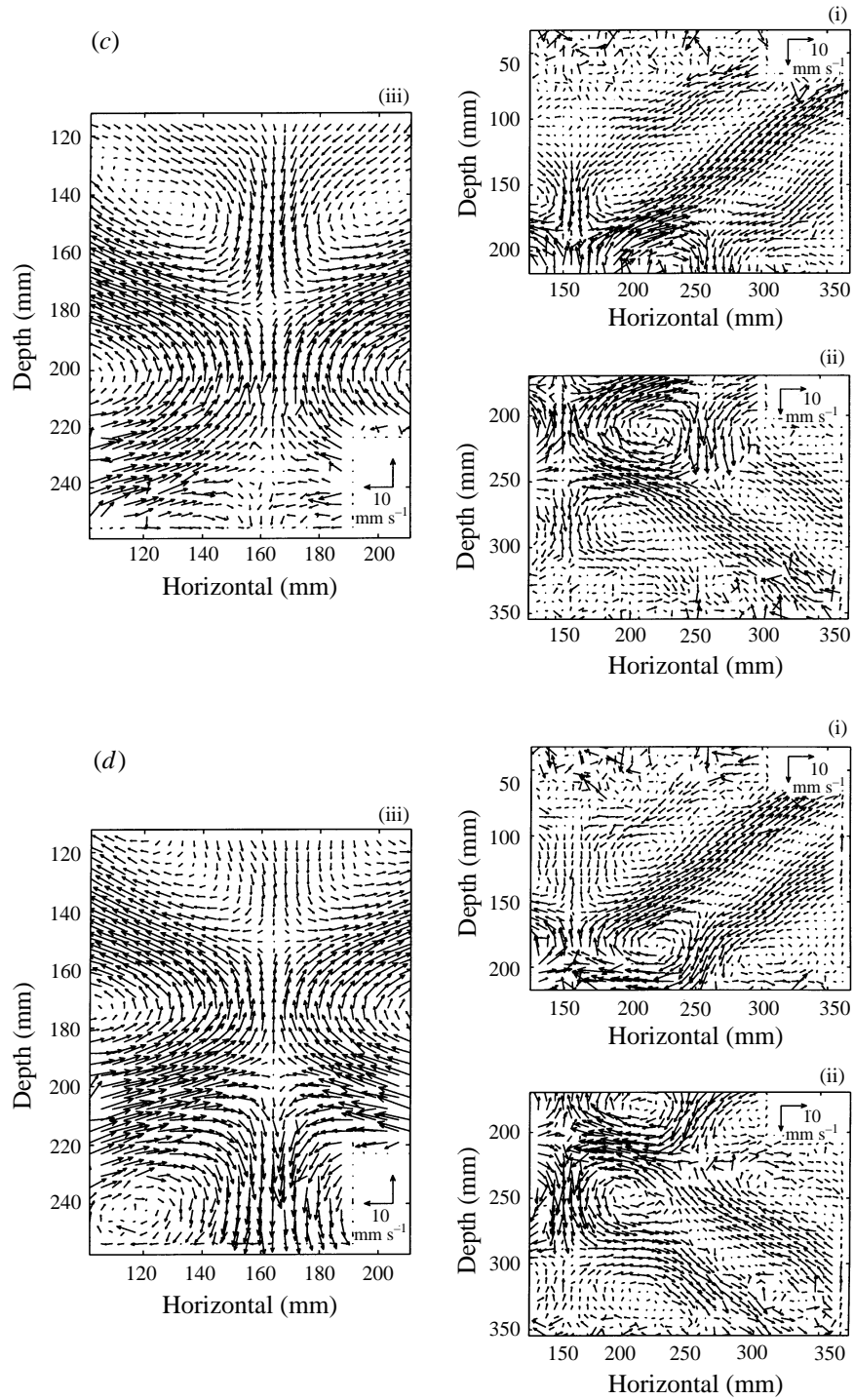


FIGURE 14. Velocity images within (i) the incoming ray, (ii) the outgoing ray, and (iii) the intersection. Images were taken at (a) $3.41T$, (b) $3.62T$, (c) $3.93T$, and (d) $4.14T$ from the series of experiments with the ambient buoyancy frequency $N_0 = 1.26 \text{ rad s}^{-1}$ and the wave frequency $f = 0.65 \text{ rad s}^{-1}$, making $f/N_0 = 0.51$. The velocity scales were plotted in the blank areas, where a clock was displayed during



the acquisition. Within velocity images, there were points without velocity vectors. These were caused by bad vectors identified during image post-processing using the multiple-passed method described by Stevens & Coates (1994). For clarity, these two-dimensional velocity fields only display velocities at interval of 20×20 pixels (3.9 mm horizontally \times 3.8 mm vertically).

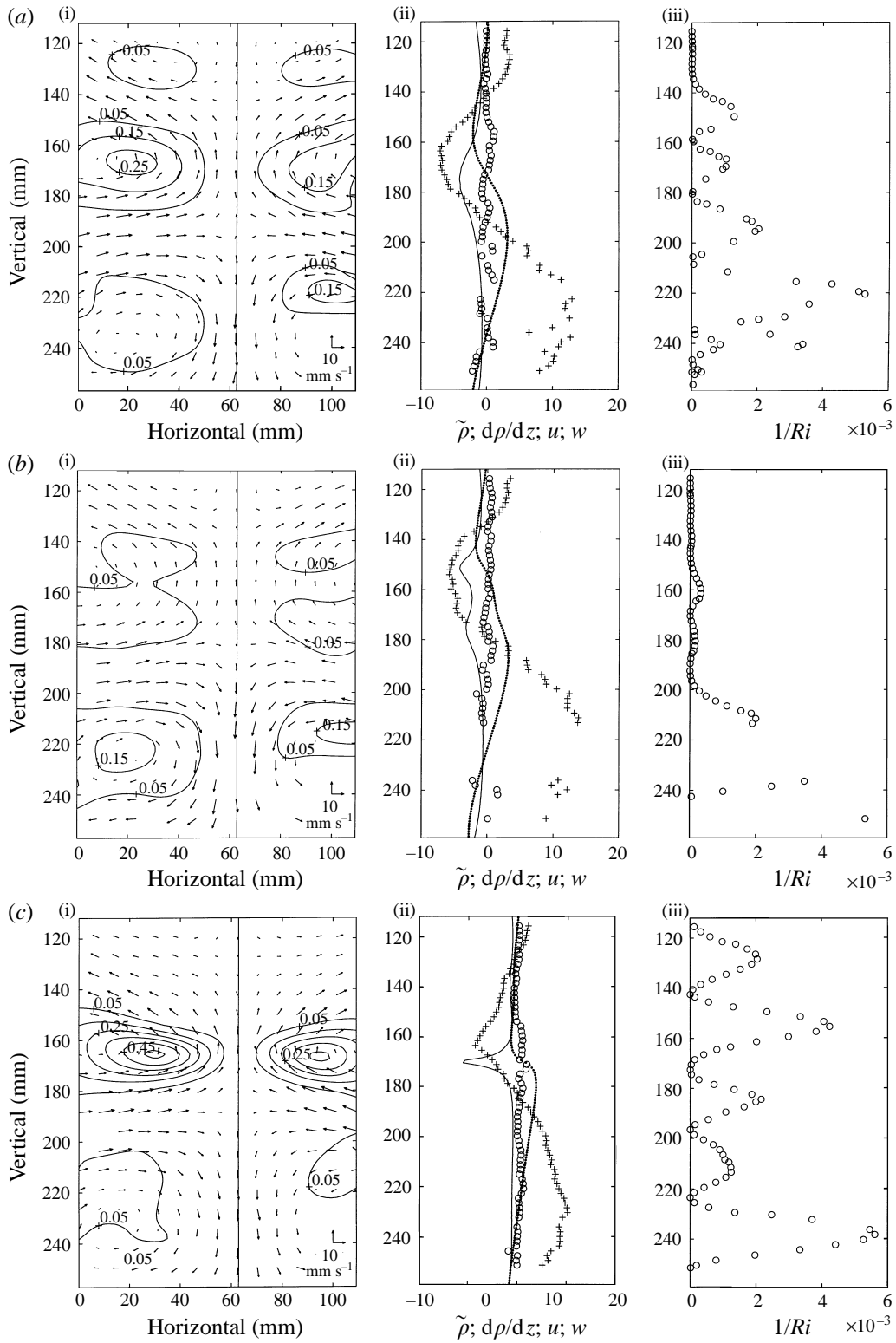


FIGURE 15(a-c). For caption see page 110.

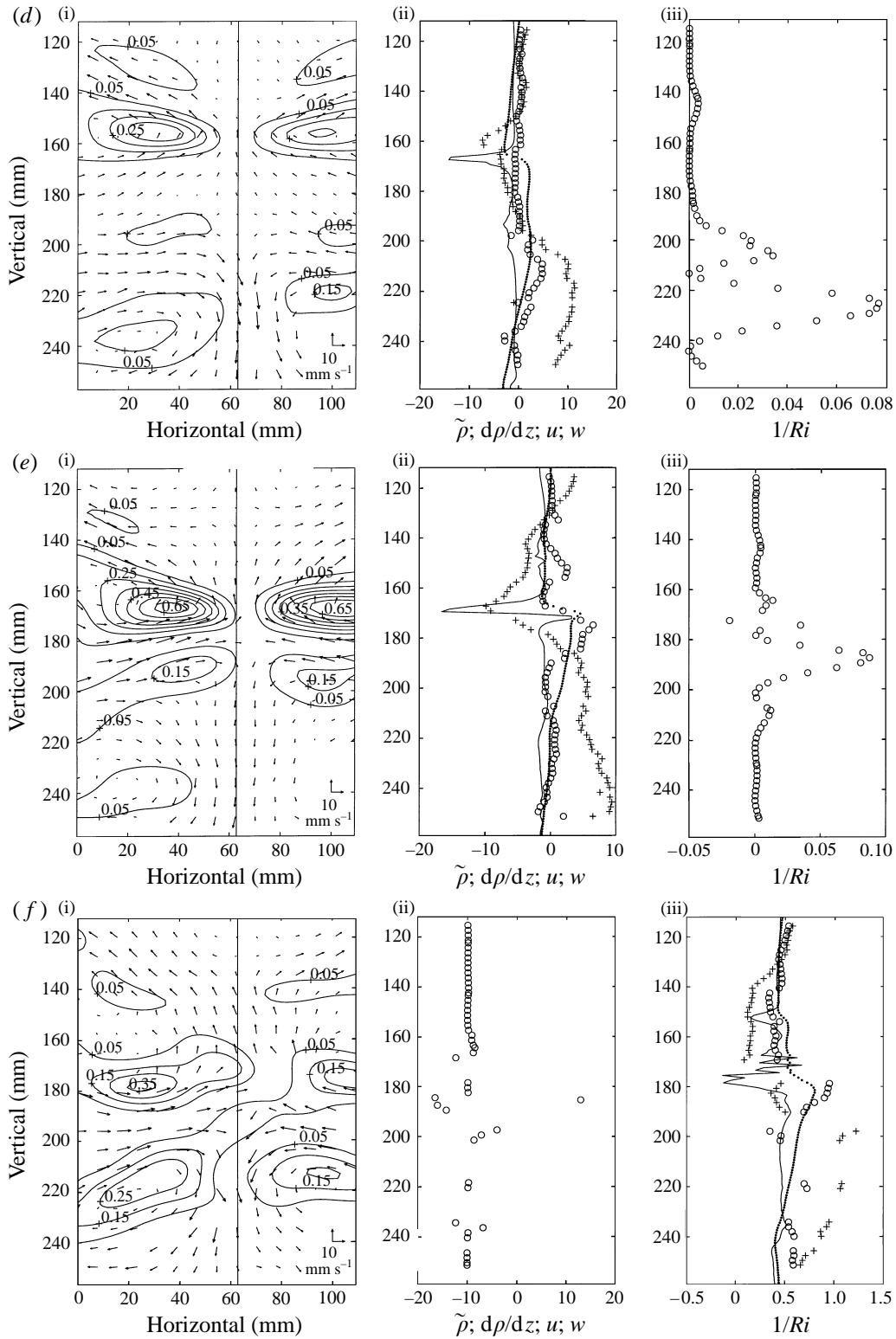


FIGURE 15(d-f). For caption see next page.

displacements. Once the isopycnals had overturned, wave energy could be transferred to the gravitationally unstable overturning which, in turn, generated turbulence.

6. Evolution of turbulence

6.1. Distribution of g' and L_c

Figures 16 and 17 illustrate a series of vertical profiles of the buoyancy anomaly g' and the centred displacement scale L_c . They (and the subsequent figures) were derived from the density profiles in figure 9 taken during $14.1T$ and $17.45T$ using the method described in Imberger & Boashash (1986), Luketina (1987) and Luketina & Imberger (1989). The buoyancy anomaly g' was defined as $g' = g(\rho - \rho_m)/\rho_0$ where ρ , ρ_m and ρ_0 were the local density, the density from the monotonized profile and the average density, respectively. The centred displacement scale L_c and the Thorpe displacement L_d (Thorpe 1977; Dillon 1982) were of the same order; they described the overturn scales registered in an instantaneous density profile. In the derivation of g' and L_c , the minimum density difference in re-ordering the density profile was 0.0159 kg m^{-3} while the resolution of density measurement was 0.0055 kg m^{-3} . Profiles in figure 16 suggested that the largest g' occurred during $14.26T$ to $14.51T$ and the subsequent g' was smaller. Figure 17 illustrates that large L_c occurred in phase with large g' .

The distributions of g' and L_c within the turbulent patch in each instantaneous vertical profile can be described by their standard deviation σ and skewness S . The skewness for the distribution of a variable ξ is defined as (e.g. Tennekes & Lumley 1972)

$$S \equiv \frac{\overline{(\xi - \bar{\xi})^3}}{\sigma^3}, \quad (3)$$

where $\bar{\xi}$ is the mean value for the variable ξ . The turbulent patch in each instantaneous vertical profile was defined here as the segment between the first and the last non-zero g' .

Figures 18(a) and 19(a) illustrate the temporal evolution of the maximum, mean and median values of g' and L_c derived from the instantaneous vertical profiles while figures 18(b, c) and 19(b, c) show the normalized standard deviation σ_n and the skewness S . The figures show that the distribution of g' and L_c were highly skewed towards values below their mean which, in turn, were small.

The timescale for an unstable overturn to collapse under buoyancy to its equilibrium level is of the order of $(\hat{g}'/\hat{L}_c)^{-1/2}$, where \hat{g}' is the instantaneous r.m.s. value of g' and \hat{L}_c is the instantaneous r.m.s. value of L_c within the turbulent patch (Imberger 1994). On the other hand, the timescale for a vertically displaced fluid element to oscillate

FIGURE 15. (i) Velocity images and $1/Ri_0$ contours at (a) $6.2T$, (b) $8.3T$, (c) $10.2T$, (d) $12.2T$, (e) $13.2T$, and (f) $14.3T$ from the experiment with the ambient buoyancy frequency $N_0 = 1.26 \text{ rad s}^{-1}$ and the wave frequency $f = 0.65 \text{ rad s}^{-1}$, making $f/N_0 = 0.51$. Contour levels were 0.05, 0.15, 0.25, 0.35, 0.45, 0.55 and 0.65. (ii) Horizontal velocity (mm s^{-1}) (○) and vertical velocity (mm s^{-1}) (+) profiles extracted from velocity image together with the density fluctuations (kg m^{-3}) (dotted line) and density gradient ($\text{kg m}^{-3} \text{ per cm}$) (solid line). The velocity scales on panel (i) were plotted in the blank area at the bottom right-hand corner. For clarity, these two-dimensional velocity fields only display velocities at interval of 40×40 pixels ($7.8 \text{ mm horizontally} \times 7.6 \text{ mm vertically}$), although velocities were computed for 10×10 pixels ($1.95 \text{ mm horizontally} \times 1.91 \text{ mm vertically}$). Nonetheless, the velocity profiles on panel (ii) display all velocities calculated, except those deemed to be bad vectors. The solid vertical lines in velocity images show the path of corresponding vertical density profiles, which were also in the plane of illumination. (iii) Vertical profile of $1/Ri$.

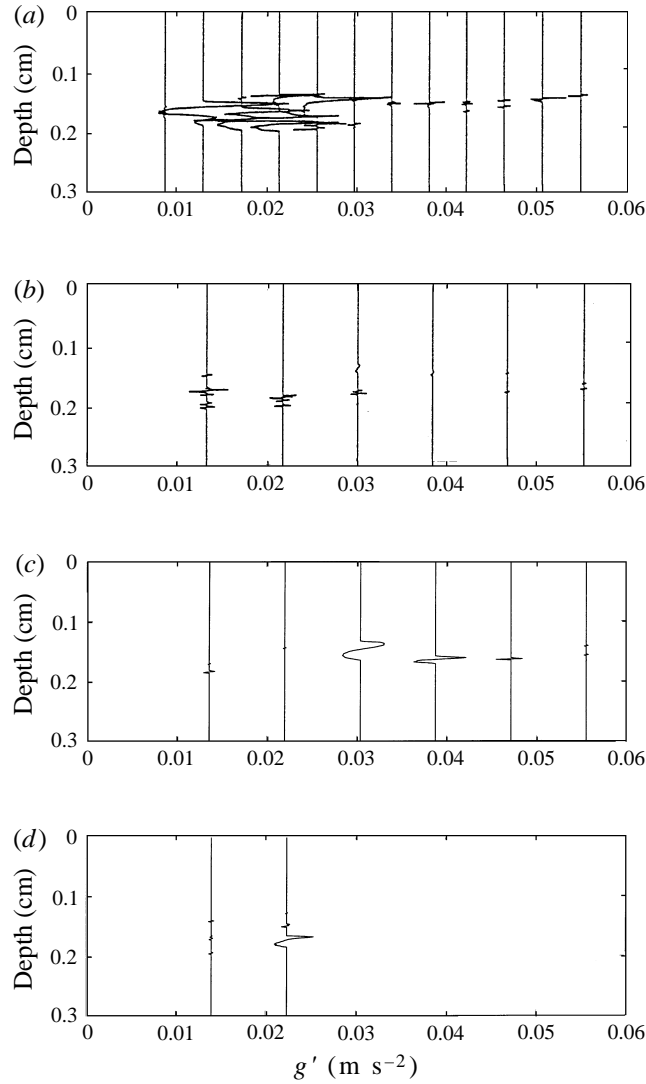


FIGURE 16. Vertical profiles of density anomaly g' taken (a) during 14.17*T* to 15.10*T*, (b) during 15.27*T* to 16.10*T*, (c) during 16.27*T* to 17.11*T*, and (d) during 17.28*T* to 17.45*T*. Profiles in (a) were at $(0.08 \pm 0.01)T$ interval apart and profiles in (b), (c) and (d) were at $(0.17 \pm 0.01)T$ interval apart. Profiles were offset by constants proportional to time interval apart.

about its initial equilibrium level under gravitational adjustment is of order of N_0^{-1} (e.g. Turner 1973). Thus, the ratio $(\hat{g}'/N_0^2 \hat{L}_c)$ can be interpreted as the square of the ratio of the gravitational adjustment time to the collapse timescale of the overturning. If $(\hat{g}'/N_0^2 \hat{L}_c) < (f^2/N_0^2)$, then the collapse of the overturning is disrupted by the wave motions, which have frequency f or higher. Figure 20 shows that $(\hat{g}'/N_0^2 \hat{L}_c)$ was always less than one. The time average of $(\hat{g}'/N_0^2 \hat{L}_c)$ was in fact 0.17, smaller than the square of the ratio of forcing frequency to buoyancy frequency $(f^2/N_0^2) = 0.23$. As a result, the release of available potential energy (APE) locked inside the overturning was strongly affected by the wave motion.

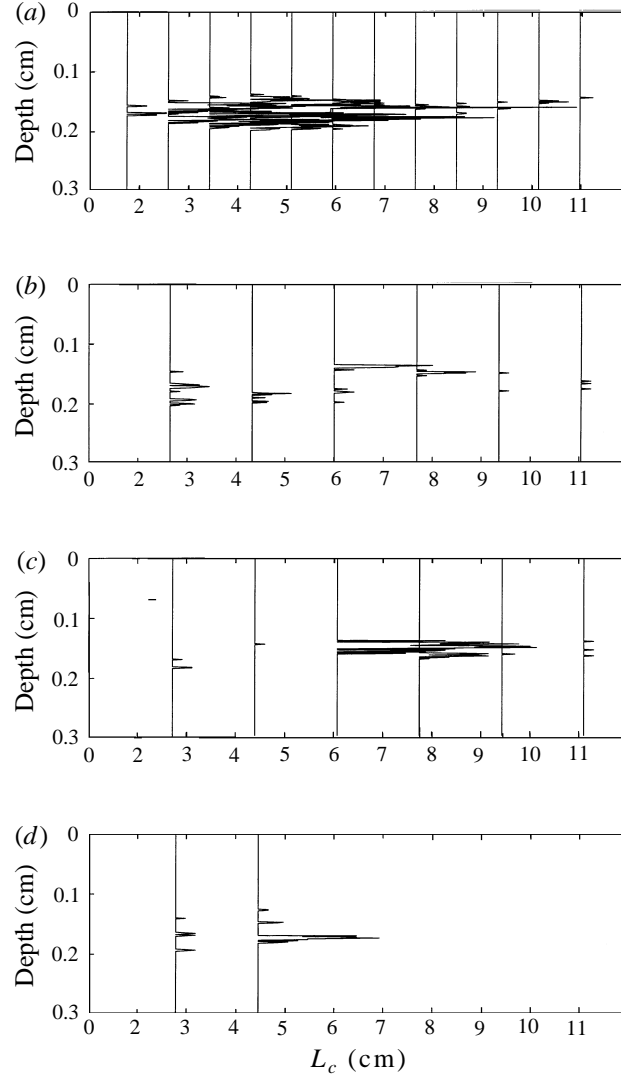


FIGURE 17. Vertical profiles of centred displacement scale L_c taken (a) during $14.17T$ to $15.10T$, (b) during $15.27T$ to $16.10T$, (c) during $16.27T$ to $17.11T$, and (d) during $17.28T$ to $17.45T$. Profiles in (a) were at $(0.08 \pm 0.01) T$ interval apart and profiles in (b), (c) and (d) were at $(0.17 \pm 0.01) T$ interval apart. Profiles were offset by constants proportional to time interval apart.

6.2. Energetics

Following II and Imberger (1994), the turbulent Froude number Fr_t , the turbulent Reynolds number Re_t and the turbulent Grashof number Gr_t are defined as

$$Fr_t = \left(\frac{\epsilon}{\hat{g}'^{3/2} \hat{L}_c^{1/2}} \right)^{1/3} = \left(\frac{L_R}{\hat{L}_c} \right)^{2/3}, \quad (4)$$

$$Re_t = \left(\frac{\epsilon \hat{L}_c^4}{\nu^3} \right)^{1/3} = \left(\frac{\hat{L}_c}{L_k} \right)^{4/3}, \quad (5)$$

$$Gr_t = \left(\frac{\hat{g}' \hat{L}_c^3}{\nu^2} \right), \quad (6)$$

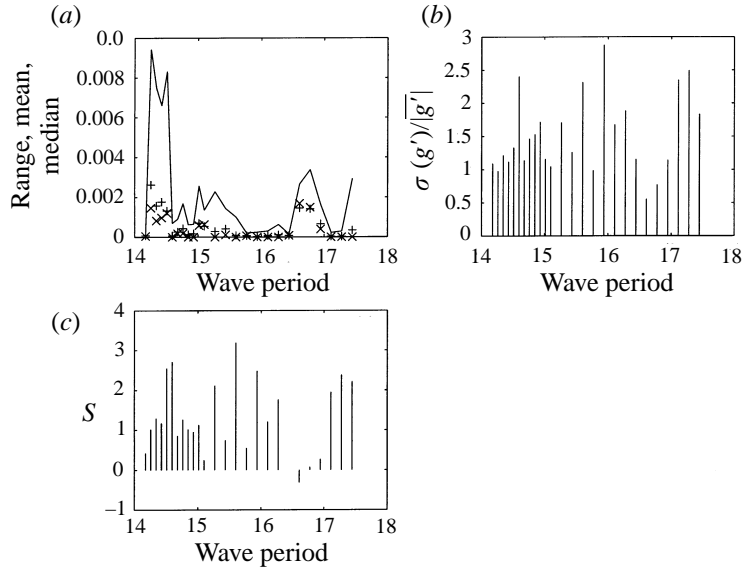


FIGURE 18. (a) The temporal evolutions of the maximum (solid line), mean (+) and median (\times) of absolute density anomaly g' (m s^{-2}). (b) The temporal evolutions of the standard deviation σ of the distribution of absolute density anomaly g' normalized by the instantaneous mean. (c) The temporal evolutions of the skewness S of the same distribution.

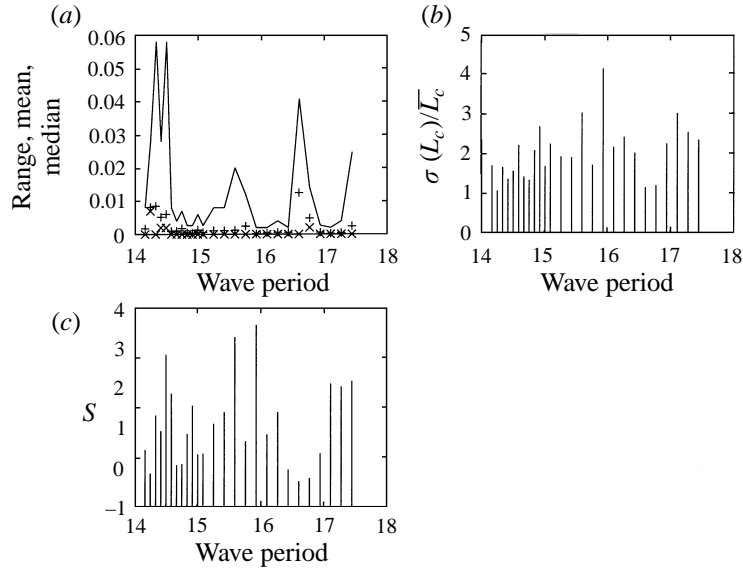


FIGURE 19. (a) The temporal evolutions of the maximum (solid line), mean (+) and median (\times) of centred displacement scale L_c (m). (b) The temporal evolutions of the standard deviation σ of the distribution of centred displacement scale L_c normalized by the instantaneous mean. (c) The temporal evolutions of the skewness S of the same distribution.

where $L_R = (e^{2/3} \hat{L}_c / \hat{g}')^{3/4}$. If $(\hat{g}' / N_0^2 \hat{L}_c) = 1$, L_R becomes equal to the Ozimov scale L_O .

The instantaneous TKE dissipation rate ϵ for a turbulent patch was obtained by curve-fitting the theoretical Batchelor spectrum for the temperature gradient (Batchelor

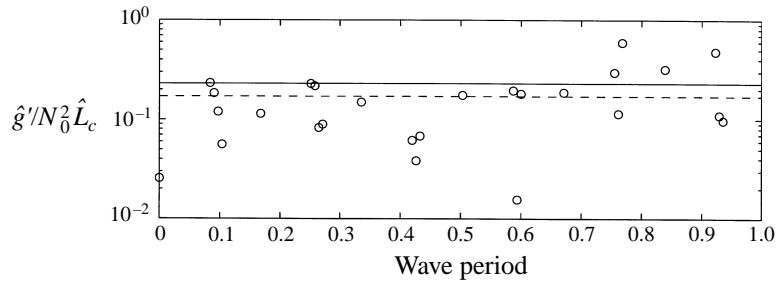


FIGURE 20. Temporal evolution of $(\hat{g}'/N_0^2 \hat{L}_c)$. The solid line is $(\hat{g}'/N_0^2 \hat{L}_c) = (f^2/N_0^2) = 0.23$ where f is the wave forcing frequency. The dashed line is $(\hat{g}'/N_0^2 \hat{L}_c) = 0.17$ which is the mean of all $(\hat{g}'/N_0^2 \hat{L}_c)$. Phase zero refers to the time of overturning at $14.17T$.

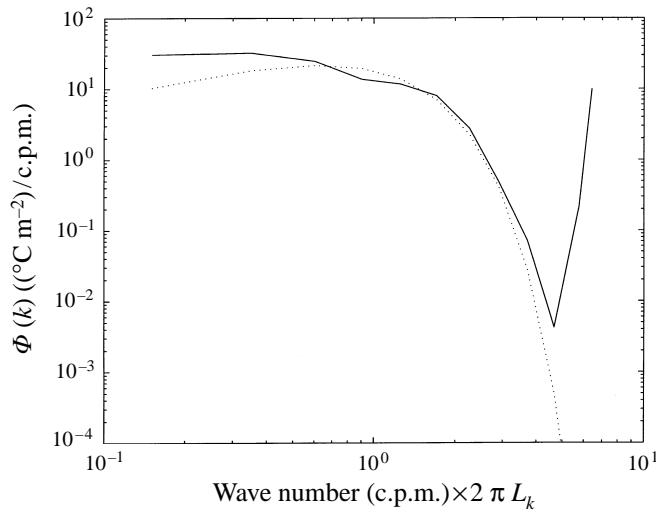


FIGURE 21. —, A typical measured temperature gradient spectrum taken at $16.27T$ and \cdots , the theoretical Batchelor spectrum. Wavenumber on the horizontal axis is normalized by the Kolmogorov scale.

1959) to the spectra from temperature measurements as described in detail by Luketina (1987) (see also Dillon & Caldwell 1980; Fozdar *et al.* 1985; Imberger & Boashash 1986; Luketina & Imberger (1980). Etemad-Shahidi & Imberger (1996) have shown from field data that the validity of this method is not limited to high Re_t . A comparison of dissipation calculations from this method with those from velocity microstructure were closely correlated for rates of dissipation in the range 10^{-8} – 10^{-5} $\text{m}^2 \text{s}^{-3}$ (see also Oakey 1982). In the present experiment, the patches having ϵ outside this range were excluded in figures 22, 24, 25 and 26. A typical temperature gradient spectrum calculated from instantaneous temperature gradient between depths 101 mm and 228 mm (total of 128 samples) is shown in figure 21. The nonlinear curve fitting of the data to the Batchelor spectrum (Luketina 1987) began from the high-wavenumber region and any contamination of the low-wavenumber portion by wave motion had minimal influence on the dissipation estimation.

The variation of the instantaneous TKE dissipation rate ϵ , normalized by νN_0^2 , is shown in figure 22. The figure shows that $(\epsilon/\nu N_0^2)$ was always less than one and the time average of $(\epsilon/\nu N_0^2)$ was 0.34. Given that $(f^2/N_0^2) = 0.23$, the Kolmogorov timescale $t_k = (\nu/\epsilon)^{1/2} \text{ rad s}^{-1}$ was $O(f^{-1})$ and larger than N_0^{-1} , meaning even the dissipative

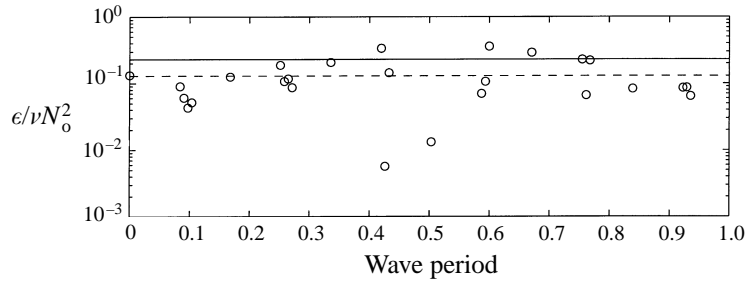


FIGURE 22. Temporal evolution of $(\epsilon/\nu N_0^2)$. The solid line is $(\epsilon/\nu N_0^2) = (f^2/N_0^2) = 0.23$ where f is the wave forcing frequency. The dashed line is $(\epsilon/\nu N_0^2) = 0.34$ which is the mean of all $(\epsilon/\nu N_0^2)$. Phase zero refers to the time of overturning at $14.17T$.

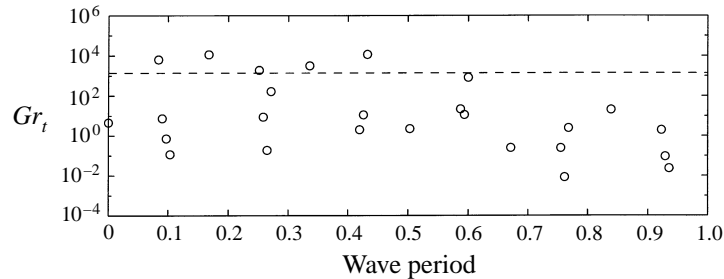


FIGURE 23. Temporal evolution of Gr_t . The dashed line is $Gr_t = 1.4 \times 10^3$ which is the mean of all Gr_t . Phase zero refers to the time of overturning at $14.17T$.

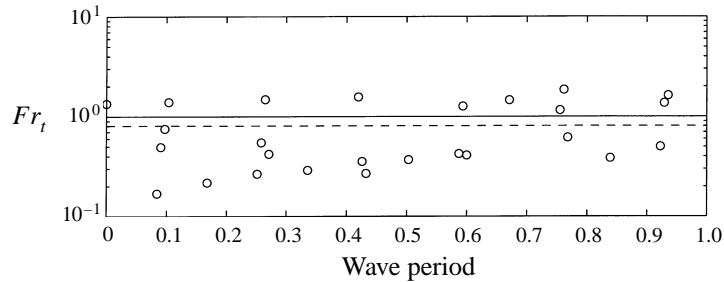


FIGURE 24. Temporal evolution of Fr_t . The solid line is $Fr_t = 1$. The dashed line is $Fr_t = 1.2$ which is the mean of all Fr_t . Phase zero refers to the time of overturning at $14.17T$.

scales were directly influenced by the wave motion and the ambient stratification. Figures 23–25 show the temporal evolution of Gr_t , Fr_t and Re_t computed as in equations (4)–(6). The range for Gr_t was from 8×10^{-3} to 1.2×10^4 , for Fr_t from 0.2 to 2.4, and for Re_t from 0.2 to 33. Gr_t and Re_t oscillated weakly with the phase of the wave cycle, although Fr_t appeared uncorrelated with the phase. The mean Gr_t was 1.4×10^3 , Fr_t was 1.2, and Re_t was 7. The locations of the turbulent patches on the Fr_t – Re_t diagram are illustrated on figure 26; the boundaries for $Fr_t = 1$, $Re_t = 15$ and $Fr_\gamma = Fr_t Re_t^{1/2} = 3.9$ described by II are shown by solid lines. The location of turbulent patches was scattered within a region on the left of these boundaries and next to $Fr_\gamma = Fr_t Re_t^{1/2} \sim 1$ (dashed line).

The large value of the mean Gr_t estimate above, in combination with previous visualizations and results from the MCC technique, are all consistent with the view that

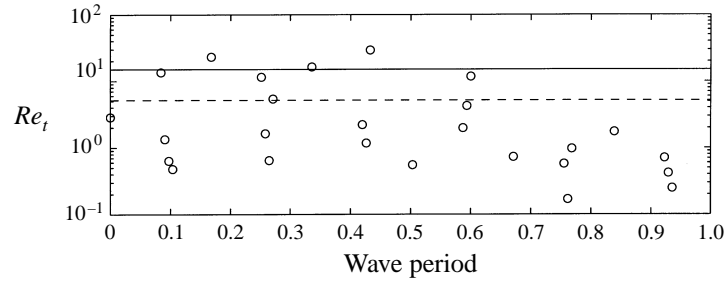


FIGURE 25. Temporal evolution of Re_t . The solid line is $Re_t = 15$. The dashed line is $Re_t = 7$ which is the mean of all Re_t . Phase zero refers to the time of overturning at $14.17T$.

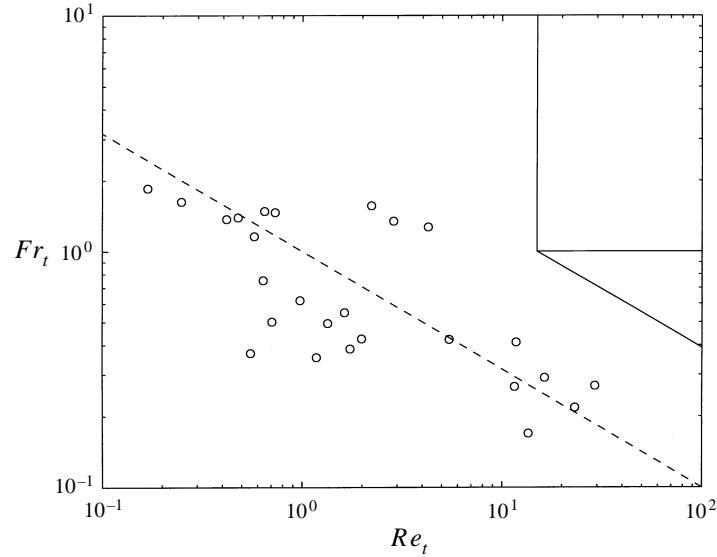


FIGURE 26. Fr_t - Re_t diagram. In the figure, the vertical solid line is $Re_t = 15$, the horizontal solid line is $Fr_t = 1$, the inclined solid line is $Fr_\gamma = Fr_t Re_t^{1/2} = 3.9$, and the inclined dashed line is $Fr_\gamma = 1$.

the overturning was gravitationally unstable. The overturning would release its potential energy to energize small-scale processes, although the release of APE was disrupted by the wave motions. Since the mean turbulent Froude number \overline{Fr}_t was $O(1)$, the maximum rate of release of APE was, on average, comparable to the TKE dissipation rate (cf. Taylor 1992).

7. Discussion

The preceding results (and the numerical results reported by Javam *et al.* 1997*b*) have confirmed that two downward propagating rays, with sufficiently large amplitudes, can interact non-resonantly and transfer some energy nonlinearly from the forcing mode to evanescent modes. The transfer of energy towards higher frequencies can also occur in nonlinear interactions between an incident and a reflected internal wave from a sloping boundary (Thorpe 1987*a*) or in the interactions near a turning point of a ray propagating against a steady shear (Javam *et al.* 1997*a*). In contrast, wave energy is transferred towards lower frequencies in the triad resonant interactions observed by Martin *et al.* (1969, 1972), in the parametric subharmonic instability

observed by McEwan & Robinson (1975) and Thorpe (1994*c*), and near a turning point of a ray propagating in an environment which has spatially varying buoyancy frequency (Javam *et al.* 1997*a*).

Since the evanescent modes cannot propagate, wave energy that has been transferred to these modes was trapped within the intersection, leading to larger localized isopycnal displacements; the vertical wavelength of the primary resultant wave, however, remained the same. Therefore, at some point, the isopycnals are forced to overturn above the stagnation point by the variations in depth in $\partial u/\partial x$ (i.e. the rate of change of horizontal velocity with horizontal distance). The increase in isopycnal displacements and the overturning of the isopycnals can also clearly be seen in the numerical simulations by Javam *et al.* (1997*b*). The increase in isopycnal slope was theoretically predicted by McEwan (1973) and, as in this earlier study, the Richardson number is larger than 0.25 preceding the overturning, although the properties of the two rays in McEwan's (1973) experiments are different. While Richardson numbers are large, the turbulent Grashof number for the overturning is large, and all these observations thus indicate the overturning is gravitationally unstable.

The mechanism leading to the overturning described above is different from that discussed by Delisi & Orlanski (1975) and Thorpe (1994*a, b*). Delisi & Orlanski (1975) investigated the overturning of isopycnals as an incident ray is reflected at a horizontal density jump. When the horizontal advection of density is larger than the horizontal phase velocity, the isopycnals near the density jump overturn (see also Orlanski & Bryan 1969; Javam *et al.* 1997*a*). Thorpe (1994*a, b*) discussed the generation of the unstable density structure in a ray. When the ray is forced at large amplitude, the heavy fluid slides above the light fluid along the ray; hence, an unstable density field is produced. In this case, the amplitude is not constrained by the wavelength of the ray, but ultimately by the unstable buoyancy field that forces the density structure to collapse.

The displacement scales registered in an instantaneous density profile are the consequences of overturning of isopycnals. Itsweire & Helland (1989) have concluded that, in actively mixing turbulence (cf. Gibson 1986) in salt stratified water, the smallest scale of motions contributing to buoyancy flux is of the order of $3L_k$, while motions at scales of the order of $18.5L_k$ contribute the most to buoyancy flux. Therefore, the skewness of the distribution of the overturning scales must somehow reflect on the dynamics of small-scale mixing. Here the distribution of L_c has a small bandwidth and is skewed towards L_k throughout the wave cycle. Further, the mean Re_t of 7 suggests that, on average, $L_c \approx 4.3L_k$. Thus, the range of scales supporting buoyancy flux is narrow and the mixing efficiency would be negligibly small. Preliminary analysis of data collected from lakes also indicates high skewness events have low mixing efficiency, and the relation between the skewness and mixing efficiency is currently under investigation. Note that the skewness should also reflect the turbulence generating mechanism as the larger displacement scales, which depend on the mechanism, are influencing the value of skewness.

Employing the laboratory results from Stillinger *et al.* 1983), Itsweire, Helland & Van Atta (1986), Lienhard & Van Atta (1990), Rohr *et al.* (1988) and Ivey & Nokes (1989), II proposed the following: when $Fr_t = (L_0/\hat{L}_c)^{2/3} = O(1)$, the turbulent motions would induce a net buoyancy flux when the square of the strain Froude number $(\epsilon/\nu N_0^2) = (L_0/L_k)^{4/3}$ is above a critical value (see also Gibson 1986). Although the critical value remains unclear (e.g. Huq & Stretch 1995), II recommended that it is about 15. At this critical $\epsilon/\nu N_0^2$, L_0 is about $7.6L_k$ or $O(10L_k)$ where the TKE spectrum starts rolling off (e.g. Tennekes & Lumley 1972). The results in §6.2 show that the mean

turbulent Froude number is $O(1)$ and $\epsilon/\nu N_0^2 < 1$. Thus, the previous results would again imply the turbulent motions had created negligible buoyancy flux. However, the motions are dissipative as indicated by the observation that the spectra for the temperature gradient are consistent with the Batchelor spectrum.

The Ozmidov scale L_o is often regarded as the energy-containing scales (e.g. Gargett *et al.* 1984; Gargett 1988; Gibson 1991). By definition, the buoyancy force is balanced by the inertial forces (as defined by ϵ) at the Ozmidov scale (e.g. Itsweire *et al.* 1986; Imberger 1994). This interpretation has assumed (or implied) the turbulent velocity scale $u = (\epsilon L_o)^{1/3}$ which is valid only for $Fr_t = (\epsilon/N_0^3 \hat{L}_c^2)^{1/3} < 1$ and $(\epsilon/\nu N_0^2) > 10$ (cf. Ivey *et al.* 1996); the latter constraint simply implies that the energy-containing scales need to be about six times larger than the Kolmogorov scales. Further, the results described in §6.2 show that $(\epsilon/\nu N_0^2)$ can be less than one, meaning L_o is less than L_k . As the Kolmogorov scale L_k is of the order of the smallest scale at which turbulent velocity fluctuations existed (e.g. Tennekes & Lumley 1972), the Ozmidov scale has no physical interpretation in terms of the velocity spectrum when $(\epsilon/\nu N_0^2) < 1$.

Sometimes, the energy-containing scales are assumed to be comparable to the overturning scales obtained from density measurements when the latter are smaller than L_o (e.g. Gregg 1987; Luketina & Imberger 1989; Taylor 1992). However, the results demonstrate that the Re_t can be less than one, meaning \hat{L}_c is smaller than L_k . Hence, \hat{L}_c deviates from the energy-containing scales as $Re_t \rightarrow 1$, eventually resulting in $Re_t < 1$. The correlation between turbulent density fluctuations and the vertical turbulent velocity fluctuations (i.e. buoyancy flux) should thus be very low as $Re_t \rightarrow 1$.

The question of whether the mechanism observed in the present experiment is generating some turbulent patches in a thermocline below the surface mixing layer (e.g. Imberger 1985) or elsewhere in the interior of a stratified lake or ocean remains unclear, although internal wave rays are ubiquitous inside these water bodies. On the other hand, Yamazaki (1990) has confirmed that the dynamics of turbulence in the laboratory experiments by Itsweire *et al.* (1986) are identical to that in the thermocline when $(\epsilon/\nu N_0^2) < 100$; thus, the critical dissipation rate $(\epsilon/\nu N_0^2) \approx 15$ from the laboratory experiments should be applicable to the thermocline. Further, when the internal wave spectrum in the thermocline is close to the Garrett & Munk spectrum (Garrett & Munk 1975), Wesson & Gregg (1994) estimated that $(\epsilon/\nu N_0^2) = 13$. Indeed, turbulent events with $O(1) < (\epsilon/\nu N_0^2) < 20$ are not uncommon in the ocean thermocline (e.g. Peters & Gregg 1988; Gregg 1989; Yamazaki 1990) and, as in the present study, they cannot sustain a net buoyancy flux.

In lakes, preliminary results have shown that many turbulent patches inside the thermocline have the characteristics of those observed in the experiments: they have high skewness S , $Re_t < 1$ and $(\epsilon/\nu M^2) < 1$, where M is the buoyancy frequency computed from the monotonized density profile. The implication is that while these events probably generate a very small buoyancy flux, they must play an important role in dissipating TKE in the interior and hence in the hydrodynamics of a lake.

8. Conclusion

The consequences of nonlinear non-resonant interactions between the two downward propagating internal wave rays were investigated. The results indicated that some wave energy was accumulated inside the interaction region owing to the production of evanescent modes. As a result, the local isopycnal displacements were increased, but the vertical wavelength of the primary resultant wave remained unchanged. Eventually, the isopycnals overturned, releasing available potential energy

and generating turbulence. Inside the turbulent patch, the distribution of the centred displacement scales was highly skewed towards the Kolmogorov scale, the turbulent Reynolds number Re_t was low, and the square of the strain Froude number ($\epsilon/\nu N_0^2$) was less than one. This suggests that almost all turbulent kinetic energy was locally dissipated and a negligible amount of mixing resulted.

We are grateful to Greg Lawrence, Prabhath DeSilva, and Abdollah Javam for discussions on this work. Also, we thank Michael Coates for the use of his MCC routines, and John Devitt, Bill Foster, Wlodek Bzdyl, and Arnold Baksas for construction and advice on the mechanical and the electronics equipment. This work is supported by the Australian Research Council. During this work, S.G.T. was a recipient of the Merit Scholarship from the Australian International Development Assistance Bureau, and a Centre for Water Research Scholarship from the Centre for Environmental Fluid Dynamics.

This paper is Centre for Water Research reference ED 894 ST.

REFERENCES

- BACHELOR, G. K. 1959 Small-scale variation of convected quantities like temperature in a turbulent fluid. Part 1. General discussion and the case of small conductivity. *J. Fluid Mech.* **5**, 113–133.
- CACCHIONE, D. & WUNSCH, C. 1974 Experimental study of internal wave spectra and mixing. *J. Phys. Oceanogr.* **15**, 1145–1156.
- DELISI, D. P. & ORLANSKI, I. 1975 On the role of density jumps in the reflexion and breaking of internal gravity waves. *J. Fluid Mech.* **69**, 445–464.
- DILLON, T. M. 1982 Vertical overturns: a comparison of Thorpe and Ozmidov length scales. *J. Geophys. Res.* **87**, 9601–9613.
- DILLON, T. M. & CALDWELL, D. R. 1980 The Batchelor spectrum and dissipation in the upper ocean. *J. Geophys. Res.* **85**, 1910–1916.
- ETEMAD-SHAHIDI, A. & IMBERGER, J. 1996 Anatomy of turbulence in thermally stratified lakes. *J. Phys. Oceanogr.* (in preparation).
- FORTUIN, J. 1960 Theory and application of two supplementary methods of constructing density gradient columns. *J. Polymer Sci.* **44**, 505–515.
- FOZDAR, M. F., PARKER, G. J. & IMBERGER, J. 1985 Matching temperature and conductivity sensor response characteristics. *J. Phys. Oceanogr.* **15**, 1557–1569.
- GARGETT, A. E. 1988 The scaling of turbulence in the presence of stable stratification. *J. Geophys. Res.* **93**, 5021–5036.
- GARGETT, A. E., OSBORN, T. R. & NASMYTH, P. W. 1984 Local isotropy and the decay of turbulence in a stratified fluid. *J. Fluid Mech.* **144**, 231–280.
- GARRET, C. & MUNK, W. 1975 Space–time scales of internal waves: a progress report. *J. Geophys. Res.* **80**, 291–297.
- GARRET, C. & MUNK, W. 1979 Internal waves in the ocean. *Ann. Rev. Fluid Mech.* **11**, 339–369.
- GIBSON, H. C. 1986 Internal waves, fossil turbulence, and composite ocean microstructure spectra. *J. Fluid Mech.* **168**, 89–117.
- GIBSON, H. C. 1991 Laboratory, numerical, and oceanic fossil turbulence in rotating and stratified flows. *J. Geophys. Res.* **96**, 12549–12566.
- GREGG, M. 1987 Diapycnal mixing in the thermocline: a review. *J. Geophys. Res.* **92**, 5249–5286.
- GREGG, M. 1989 Scaling turbulent dissipation in the thermocline. *J. Geophys. Res.* **94**, 9686–9698.
- HASSELMANN, K. 1967 A criterion for nonlinear wave stability. *J. Fluid Mech.* **30**, 737–739.
- HEAD, M. J. 1983 The use of miniature four-electrode conductivity probes for high resolution measurement of turbulent density or temperature variations in salt-stratified water flows. PhD dissertation, University of California, San Diego.
- HOPFINGER, E. J. 1987 Turbulence in stratified fluids: a review. *J. Geophys. Res.* **92**, 5287–5303.
- HOWES, W. L. 1984 Rainbow schlieren and its application. *Appl. Optics* **23**, 2449–2460.

- HUO, P. & STRETCH, D. D. 1995 Critical dissipation rates in density stratified turbulence. *Phys. Fluids* **7**(5), 1034–1039.
- IMBERGER, J. 1985 The diurnal mixed layer. *Limnol. Oceanogr.* **30**, 737–770.
- IMBERGER, J. 1994 Transport processes in lakes: a review article. In *Limnology Now: A Paradigm of Planetary Problems* (ed. R. Margalef), pp. 99–193.
- IMBERGER, J. & BOASHASH, B. 1986 Application of the Wigner–Ville distribution to temperature gradient microstructure: a new technique to study small-scale variations. *J. Phys. Oceanogr.* **16**, 1997–2012.
- IMBERGER, J. & IVEY, G. N. 1991 On the nature of turbulence in a stratified fluid. Part II. Application to lakes. *J. Phys. Oceanogr.* **21**, 659–680.
- ITSWEIRE, E. C. & HELLAND, K. H. 1989 Spectra and energy transfer in stably stratified turbulence. *J. Fluid Mech.* **207**, 419–452.
- ITSWEIRE, E. C., HOLLAND, K. H. & VAN ATTA, C. W. 1986 The evolution of grid-generated turbulence in a stably stratified fluid. *J. Fluid Mech.* **162**, 299–338.
- IVEY, G. N., DESILVA, I. P. D. & IMBERGER, J. 1995 Internal waves, bottom slopes and boundary mixing. In *Proceedings Aha Huliko a Hawaiian winter workshop on topographic effects in the ocean*, Honolulu, Hawaii, pp. 199–205.
- IVEY, G. N. & IMBERGER, J. 1991 On the nature of turbulence in a stratified fluid. Part I. The energetics of mixing. *J. Phys. Oceanogr.* **21**, 650–658 (referred to herein as II).
- IVEY, G. N., IMBERGER, J. & KOSEFF, J. 1996 Buoyancy fluxes in a stratified fluid. In *Physical Limnology* (ed. J. Imberger) (accepted for publication), AGU Press.
- IVEY, G. N. & NOKES, R. I. 1989 Vertical mixing due to the breaking of critical internal waves on sloping boundaries. *J. Fluid Mech.* **204**, 479–500 (referred to herein as IN).
- JAVAM, A., IMBERGER, J. & ARMFELD, S. S. 1997*a* The excitation of harmonics by nonlinear reflections of the internal waves. *J. Fluid Mech.* (submitted).
- JAVAM, A., IMBERGER, J. & ARMFELD, S. W. 1997*b* Numerical study of internal wave–wave interactions. *J. Fluid Mech.* (submitted).
- LAWRENCE, G. A., BROWAND, F. K. & REDEKOPP, L. G. 1991 The stability of a sheared density interface. *Phys. Fluids A* **3**, 2360–2370.
- LEBLOND, P. D. & MYSAK, L. A. 1978 *Waves in the Ocean*. Elsevier.
- LIENHARD, V. J. H. & VAN ATTA, C. W. 1990 The decay of turbulence in thermally stratified flow. *J. Fluid Mech.* **210**, 57–112.
- LIN, C. L., FERZIGER, J. H., KOSEFF, J. R. & MONISMITH, S. G. 1993 Simulation and stability of two-dimensional internal gravity waves in a stratified shear flow. *Dyn. Atmos. Oceans* **19**, 325–366.
- LIN, C. L., FERZIGER, J. H., KOSEFF, J. R. & MONISMITH, S. G. 1996 Single triad resonant interactions in linearly stratified fluids. *J. Fluid Mech.* (submitted).
- LOMBARD, P. N. & RILEY, J. J. 1996 On the breakdown into turbulence of propagating internal waves. *Dyn. Atmos. oceans* **23**, 345–356.
- LUKETINA, D. A. 1987 Frontogenesis of freshwater overflow. PhD thesis, University of Western Australia.
- LUKETINA, D. A. & IMBERGER, J. 1989 Turbulence and entrainment in a buoyant surface plume. *J. Geophys. Res.* **94**, 12619–12636.
- MCCOMAS, C. H. & BRETHERTON, F. P. 1977 Resonant interaction of oceanic internal waves. *J. Geophys. Res.* **82**, 1397–1412.
- MCEWAN, A. D. 1971 Degeneration of resonantly-excited standing internal gravity waves. *J. Fluid Mech.* **50**, 431–448.
- MCEWAN, A. D. 1973 Interactions between internal gravity waves and their traumatic effect on a continuous stratification. *Boundary-Layer Met.* **5**, 159–175.
- MCEWAN, A. D. 1983*a* The kinematics of stratified mixing through internal wavebreaking. *J. Fluid Mech.* **128**, 47–57.
- MCEWAN, A. D. 1983*b* Internal mixing in stratified fluids. *J. Fluid Mech.* **128**, 59–80.
- MCEWAN, A. D. & PLUMB, R. A. 1977 Off-resonant amplification of finite internal wave packets. *Dyn. Atmos. Oceans* **2**, 83–105.

- MC EWAN, A. D. & ROBINSON, R. M. 1975 Parametric instability of internal gravity waves. *J. Fluid Mech.* **67**, 667–687.
- MARTIN, S., SIMMONS, W. & WUNSCH, C. 1969 Resonant internal wave interactions. *Nature* **224**, 1014–1016.
- MARTIN, S., SIMMONS, W. & WUNSCH, C. 1972 The excitation of resonant triads by single internal waves. *J. Fluid Mech.* **53**, 17–44.
- MERZKIRCH, W. 1974 *Flow Visualization*. Academic Press.
- MOWBRAY, D. E. & RARITY, B. S. H. 1967 A theoretical and experimental investigation of the phase configuration of internal waves of small amplitude in a density stratified fluid. *J. Fluid Mech.* **78**, 1–16.
- MÜLLER, P., D'ASARO, E. A. & HOLLOWAY, G. 1991 Internal gravity waves and mixing. In *Proceedings Aha Huliko a Hawaiian Winter Workshop* (ed. P. Müller & D. Henderson), pp. 499–508.
- MÜLLER, P. & HENDERSON, D. (ed.) 1991 Dynamics of Oceanic Internal Gravity Waves. *Proceedings Aha Huliko a Hawaiian Winter Workshop*.
- MUNK, W. 1981 Internal waves and small-scale processes. In *Evolution of Physical Oceanography* (ed. B. A. Warren & C. Wunsch), pp. 264–290.
- Oakey, N. S. 1982 Determination of the rate of dissipation of turbulent energy from simultaneous temperature and velocity shear microstructure measurements. *J. Phys. Oceanogr.* **12**, 256–271.
- ORLANSKI, I. & BRYAN, B. 1969 Formation of the thermocline step structure by large-amplitude internal gravity waves. *J. Geophys. Res.* **74**, 6975–6983.
- PETERS, H. & GREGG, M. C. 1988 Some dynamical and statistical properties of Equatorial turbulence. In *Small-Scale Turbulence and Mixing in the Ocean* (ed. J. C. J. Nihoul & B. M. Jamart), pp. 185–200.
- PHILLIPS, O. M. 1968 The interaction trapping of internal gravity waves. *J. Fluid Mech.* **34**, 407–416.
- PHILLIPS, O. M. 1977 *The Dynamics of the Upper Ocean*. Cambridge University Press.
- PHILLIPS, O. M. 1991 The Kolmogorov spectrum and its oceanic cousins: a review. In *Turbulence and Stochastic Processes: Kolmogorov's Ideas 50 Years On* (ed. J. C. R. Hunt, O. M. Phillips & D. Williams), pp. 125–138. The Royal Society London.
- ROHR, J. J., ITSWEIRE, E. C., HELLAND, K. N. & VAN ATTA, C. W. 1988 Growth and decay of turbulence in a stably stratified shear flow. *J. Fluid Mech.* **195**, 77–111.
- STEVENS, C. & COATES, M. 1994 Application of a maximised cross-correlation technique for resolving velocity fields in laboratory experiments. *J. Hydraul. Res.* **32**, 195–212.
- STILLINGER, D. C., HELLAND, K. N. & VAN ATTA, C. W. 1983 Experiments on the transition of homogeneous turbulence to internal waves in a stratified fluid. *J. Fluid Mech.* **131**, 91–122.
- TAYLOR, J. 1992 The energetics of breaking events in a resonantly forced internal wave field. *J. Fluid Mech.* **239**, 309–340.
- TAYLOR, J. 1993 Turbulence and mixing in the boundary layer generated by shoaling internal waves. *Dyn. Atmos. Oceans* **19**, 233–258.
- TENNEKES, H. & LUMLEY, J. L. 1972 *A First Course in Turbulence*. MIT press.
- TEOH, S. G. 1995 Laboratory study of the interactions between two internal wave rays. PhD thesis, University of Western Australia.
- THORPE, S. A. 1966 On wave interactions in a stratified fluid. *J. Fluid Mech.* **24**, 737–751.
- THORPE, S. A. 1975 The excitation, dissipation, and interaction of internal waves in the deep ocean. *J. Geophys. Res.* **80**, 328–338.
- THORPE, S. A. 1977 Turbulence and mixing in a Scottish Loch. *Phil. Trans. R. Soc. Lond. A* **286**, 125–181.
- THORPE, S. A. 1981 An experiment study of critical layers. *J. Fluid Mech.* **103**, 321–344.
- THORPE, S. A. 1987a On the reflection of a train of finite-amplitude internal waves from uniform slope. *J. Fluid Mech.* **178**, 279–302.
- THORPE, S. A. 1987b Transitional phenomena and the development of turbulence in stratified fluids: a review. *J. Geophys. Res.* **92**, 5231–5248.
- THORPE, S. A. 1994a The stability of statically unstable layers. *J. Fluid Mech.* **260**, 315–331.

- THORPE, S. A. 1994*b* Statically unstable layers produced by overturning internal gravity waves. *J. Fluid Mech.* **260**, 333–350.
- THORPE, S. A. 1994*c* Observations of parametric instability and breaking waves in an oscillating tilted tube. *J. Fluid Mech.* **261**, 33–45.
- TURNER, J. S. 1973 *Buoyancy Effects in Fluids*. Cambridge University Press.
- WESSON, J. C. & GREGG, M. C. 1944 Mixing at Camarinal Sill in the Strait of Gibraltar. *J. Geophys. Res.* **99**, 9847–9878.
- WINTERS, K. B. & RILEY, J. J. 1992 Instability of internal waves near a critical level. *Dyn. Atmos. Oceans* **16**, 249–278.
- YAMAZAKI, H. 1990 Stratified turbulence near a critical dissipation rate. *J. Phys. Oceanogr.* **20**, 1583–1598.